Computer Methods in Applied Mechanics and Engineering 435 (2025) 117585

Contents lists available at ScienceDirect

Comput. Methods Appl. Mech. Engrg.

journal homepage: www.elsevier.com/locate/cma

A Discontinuity-Enriched Finite Element Method (DE-FEM) for modeling quasi-static fracture growth in brittle solids

Jujian Zhang [a], Yuheng Yan [b], C. Armando Duarte [c], Alejandro M. Aragón [b,*]

[a] Faculty of Civil Engineering and Geosciences, Delft University of Technology, Stevinweg 1, 2628 CN Delft, The Netherlands
[b] Faculty of Mechanical Engineering, Delft University of Technology, Mekelweg 2, 2628 CD Delft, The Netherlands
[c] Department of Civil and Environmental Engineering, University of Illinois at Urbana-Champaign, Newmark Laboratory, 205 North Mathews Avenue, Urbana, IL 61801, USA

GRAPHICAL ABSTRACT

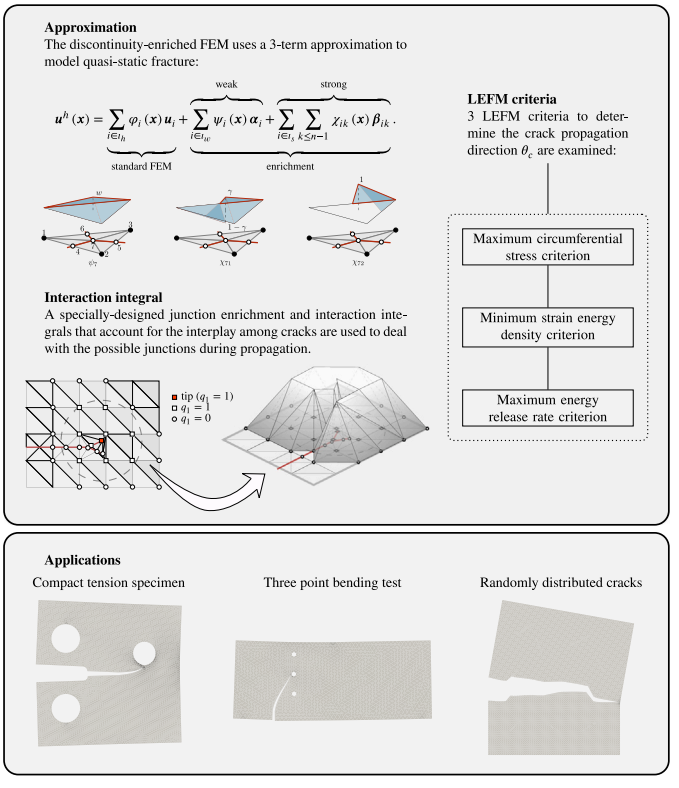

* Corresponding author.
E-mail address: a.m.aragon@tudelft.nl (A.M. Aragón).
URL: https://www.tudelft.nl/en/staff/a.m.aragon/ (A.M. Aragón).

https://doi.org/10.1016/j.cma.2024.117585
Received 13 August 2024; Received in revised form 31 October 2024; Accepted 18 November 2024
Available online 9 December 2024

ARTICLE INFO

Keywords:
Discontinuity-enriched finite element method (DE-FEM)
Brittle fracture
Quasi-static crack propagation
Interaction integral
Crack merging
Intersecting discontinuities

ABSTRACT

Enriched finite element methods (*e*-FEMs) have become a popular choice for modeling problems containing material discontinuities (e.g., multi-phase materials and fracture). The main advantage as compared to the standard finite element method (FEM) remains the versatility in the choice of discretizations, since *e*-FEMs resolve discontinuities by completely decoupling them from the finite element mesh. However, modeling complex kinematics such as branching and merging of discrete cracks remains challenging.

This article extends previous research on the Discontinuity-Enriched Finite Element Method (DE-FEM) for simulating quasi-static crack propagation in brittle materials. In DE-FEM enrichments are added to nodes created directly along discontinuities. Most notably, we demonstrate DE-FEM can resolve complex kinematics, namely the modeling of multiple cracks propagating and merging—and with a straightforward computer implementation. We validate the formulation with experimental results carried out on a compact tension specimen. Other numerical examples show the capability of DE-FEM in capturing crack paths similar to those observed in the literature.

1. Introduction

Fracture has long been of significant concern in the field of structural engineering. Cracks constitute pathways for chemical substances such as chlorides, which can compromise structural integrity [1]. Characterized by its unpredictability and abrupt growth, brittle fracture has the potential to lead to catastrophic failure without warning, thereby posing a significant hazard to human life. Therefore, it is of utmost importance to fathom the mechanisms governing brittle crack growth, for which numerical procedures have proven viable. This paper is concerned with an enriched finite element method that can be used to predict quasi-static fracture paths in brittle solids without the need for remeshing.

Numerous numerical methods have been developed to model fracture at a continuum level. Traditionally, modeling fracture has primarily relied on the finite element method (FEM). Computational fracture mechanics encountered in FEM a means to obtain predictions to problems for which there is no closed-form solution. However, standard FEM requires meshes where cracks are aligned with the faces of finite elements (i.e., fracture-fitted meshes). Furthermore, capturing the singularity of the stress field along crack fronts—as predicted by Westergaard [2]—requires special care. For instance, Tracey [3] introduced a triangular singularity finite element to better represent the stress field near the crack tip, and showed that an accurate estimation of the 2-D mode I stress intensity factor could be obtained with as few as 250 degrees of freedom (DOFs). In Tracey's finite element the singularity was obtained by emulating the displacement field of a quadrilateral finite element where two nodes were mapped from parametric space into the crack tip location in physical space. Barsoum [4] later introduced quadratic quarter-point finite elements, where the singularity is achieved by placing the middle side nodes of a quadratic element closer to the crack tip, specifically at $1/4$th of the edge length from the tip. While quarter-point finite elements can be used in conjunction with unstructured meshes in both 2-D and 3-D to obtain accurate stress intensity factors (SIFs) [5–7], additional meshing efforts are still required for crack growth problems in order to generate fracture-fitted meshes.

The aforementioned challenges faced by the discrete fracture model implemented in standard FEM prompted researchers to propose other methodologies, in particular to avoid dealing with remeshing. Methods that use smeared models of fracture—i.e., a diffuse representation of cracks over finite elements—are growing in popularity due to their ability to handle intricate crack patterns and propagation without relying on a Linear Elastic Fracture Mechanics (LEFM) criterion to determine crack growth initiation and its direction. However, traditional smeared models that consider fracture as the consequence of local material degradation, i.e., continuum-damage models, tend to result in ill-posed boundary value problems due to the loss of ellipticity [8]. The solution to this problem is highly dependent on the discretization. To overcome this drawback in the context of brittle fracture, an efficient alternative is to regularize damage by introducing an internal length scale [9,10]. Within this category, the phase-field method is a popular choice to model both quasi-static and dynamic crack propagation [11]. The method approximates the fracture surface by a phase field $c(x,t) \in [0,1]$, with $c(x,t) = 1$ indicating intact material and $c(x,t) = 0$ the crack. Together with the variational formulation for quasi-static brittle fracture based on energy minimization [12–14], the phase-field method has been widely applied to model quasi-static crack growth [15–17]. Although these diffuse-crack methods can simulate brittle fracture without the need for an LEFM criterion, the spontaneous damage evolution can sometimes lead to unrealistic fracture patterns—i.e., compression fracture due to the isotropic assumption that does not distinguish between tension and compression [18]. Furthermore, these models can only provide a diffuse representation of discontinuities that are in fact discrete. Although the phase-field model is free from the ill-posedness problem, the mesh size near the crack region is required to be fine enough to resolve the phase-field, which calls for either a globally fine mesh or adaptive mesh refinement near critical regions where cracks nucleate. In addition to the primal displacement field, additional computational cost is spent on the solution of the phase-field variables.

The representation of cracks in smeared models of fracture, while versatile for many applications, becomes problematic for others where cracks need to be described discretely. For instance, Reynolds flow models used in hydraulic fracture rely on a precise measurement of the crack opening [19,20]. For such problems smeared models would thus require additional computations to

determine displacement jumps across cracks. In addition to standard FEM, which has traditionally been a choice for representing discrete cracks, researchers have explored alternative techniques for modeling crack propagation while avoiding the substantial computational cost associated with remeshing. In the Boundary Element Method (BEM) [21] only the domain's boundary and crack surfaces are discretized into elements. BEM therefore avoids remeshing of the whole domain, although it still mandates for the subdivision of crack surfaces. In the Element-free Galerkin Method (EFGM) [22,23], the model is constructed using a cloud of points; this provides more straightforward and accurate evaluation of stress intensity factors by increasing the node density around the crack tip, and facilitates the modeling of evolving fractures by simply moving the dense nodes distribution along the crack propagation direction. Yet, these methods are no without limitations: BEM requires special measures to deal with nonlinear problems because of its dependence on Green functions. EFGM mandates for special techniques for prescribing essential boundary conditions—this is because the EFGM shape functions do not satisfy the Kronecker-δ property along Dirichlet boundaries. Furthermore, the integration of weak forms discretized with EFGM shape functions is computationally expensive and cumbersome.

Enriched finite element methods (*e*-FEMs) have also been proposed to ease the burden of a matching mesh and thus model arbitrary crack growth without remeshing. In the eXtended/Generalized Finite Element Method (X/GFEM) [24–26], the standard FEM space is enhanced by means of enrichment functions that properly describe the fracture's displacement jump kinematics (i.e., strong discontinuities) and the singularity of field gradients close to the crack front. X/GFEM has demonstrated its efficiency in single crack propagation under both quasi-static [24,25] and dynamic [26–28] settings. X/GFEM has been shown to handle complex crack patterns [29], with multiscale analysis using X/GFEM predicting the shielding and amplification effects associated with multiple crack surfaces [30,31]. Furthermore, in quasi-static multiple crack growth, it is observed that cracks tend to form 90° junctions [29,32,33]. Although X/GFEM has been successfully demonstrated for modeling complex junctions, its implementation remains challenging. It requires the use of multiple Heaviside functions at junction nodes [34] or a simpler alternative—a combination of step enrichments for junction handling [29,35].

Another family of *e*-FEMs, whereby enrichments are placed directly along discontinuities, can be derived from X/GFEM [36]. Within this family, the Interface-enriched Generalized Finite Element Method (IGFEM) was first proposed to solve problems containing weak discontinuities, i.e., problems with discontinuous gradient fields [37,38]. The method was then generalized to treat both weak and strong discontinuities with a unified three-term formulation in what was coined the Discontinuity-Enriched Finite Element Method (DE-FEM) [39–43]. Because enrichment functions vanish at standard mesh nodes, in these discontinuity-enriched formulations the standard DOFs preserve their physical meaning, and prescribing nonzero Dirichlet boundary conditions is as straightforward as in standard FEM. Because enrichments are identically zero in *blending elements*—i.e., elements that are contiguous to cut elements that blend enriched elements with the rest of the mesh—there is no degraded accuracy in these elements [44,45]. Moreover, DE-FEM can also be used as an immersed boundary method with strong enforcement of nonzero embedded essential boundary conditions and smooth reactive tractions are recovered at Dirichlet boundaries without the need for stabilization [41]. These formulations have been shown to be intrinsically stable with a proper scaling of enrichment functions or by employing a diagonal Jacobi-like preconditioner [38,40,41]. Finally, the computer implementation in displacement-based finite element codes is straightforward, and therefore DE-FEM emerges as a compelling methodology for modeling fracture. However, to date the method has only been demonstrated on static cracks.

In this article we demonstrate, for the first time, the Discontinuity-Enriched Finite Element Method for the modeling of quasi-static fracture growth in brittle materials. In particular, we highlight the ease with which DE-FEM can handle the kinematics at fracture junctions. To ensure quasi-static crack propagation, the energy release rate at the crack tip is controlled below the critical energy release rate by adjusting the loading, in accordance with Griffith's criterion [46]. We study three commonly used LEFM criteria for determining crack growth direction: namely the maximum circumferential stress [47], the minimum strain energy density [48], and the maximum energy release rate [49]. An interaction integral is employed to extract SIFs. In the context of multiple crack growth, the interaction integral is appropriately truncated based on the positions of adjacent cracks and domain boundaries to account for interaction effects and ensure accurate SIF values. The capability of DE-FEM is showcased on a series of fracture examples with single and multiple propagating cracks, all assuming small deformation kinematics. We first validate the methodology with experimental results obtained on compact tension specimens. It is shown that DE-FEM successfully recovers accurate SIF values under interaction effects, including shielding and amplification, obtaining on coarse meshes similar cracked patterns to those obtained by other numerical methods.

2. Problem description and formulation

Consider in Fig. 1 a continuous open domain $\Omega \subset \mathbb{R}^2$ with closure $\overline{\Omega}$, bounded by $\Gamma \equiv \partial\Omega = \overline{\Omega} \setminus \Omega$ with normal vector $\boldsymbol{n}_\Gamma$. Several cracks are distributed within the domain. By denoting Γ_i^C the ith crack, the set of all n_c cracks is therefore $\Gamma^C = \bigcup_{i=1}^{n_c} \Gamma_i^C \subset \Gamma$. All the cracks are considered to be traction-free. Dirichlet boundary conditions prescribe the displacement field $\bar{\boldsymbol{u}}$ on the region $\Gamma^D \subset \Gamma$. Similarly, the Neumann boundary conditions prescribe the traction $\bar{\boldsymbol{t}}$ on the region $\Gamma^N \subset \Gamma$. The boundary value problem then involves solving for the balance of linear momentum (static equilibrium) and boundary conditions, i.e.,

$$\boldsymbol{\nabla} \cdot \boldsymbol{\sigma} + \boldsymbol{b} = \boldsymbol{0} \quad \text{in } \Omega \times T, \tag{1}$$

$$\boldsymbol{u} = \bar{\boldsymbol{u}} \quad \text{on } \Gamma^D \times T, \tag{2}$$

$$\boldsymbol{\sigma} \cdot \boldsymbol{n}_\Gamma = \bar{\boldsymbol{t}} \quad \text{on } \Gamma^N \times T, \tag{3}$$

$$\boldsymbol{\sigma} \cdot \boldsymbol{n}_\Gamma = \boldsymbol{0} \quad \text{on } \Gamma^C \times T, \tag{4}$$

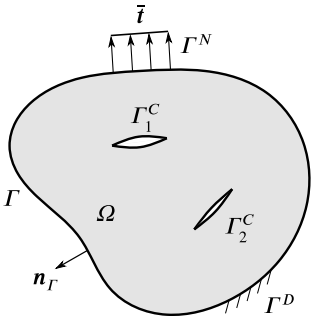

Fig. 1. A continuous body Ω with boundary Γ having unit normal $\boldsymbol{n}_\Gamma$. The body contains multiple traction-free cracks $\bigcup_{i=1}^{n_c} \Gamma_i^C \subset \Gamma$. Boundary conditions include prescribed tractions $\bar{\boldsymbol{t}}$ on Γ^N and prescribed displacements $\bar{\boldsymbol{u}}$ on Γ^D.

where T is an interval that is subdivided in quasi-static increments (pseudo-time steps), $\boldsymbol{u}(\boldsymbol{x}) : \overline{\Omega} \to \mathbb{R}^2$ denotes the displacement vector as a function of coordinate $\boldsymbol{x}$, $\boldsymbol{\sigma}(\boldsymbol{x}) : \overline{\Omega} \to \mathbb{R}^2 \times \mathbb{R}^2$ the Cauchy stress tensor, and $\boldsymbol{b}(\boldsymbol{x}) : \Omega \to \mathbb{R}^2$ the body force vector. We assume a linear relationship between stress and strain (Hooke's law) and therefore $\boldsymbol{\sigma} = \boldsymbol{C}\boldsymbol{\varepsilon}$, where $\boldsymbol{C}$ denotes the fourth-order constitutive tensor and $\boldsymbol{\varepsilon}$ is the linearized strain tensor (small deformation kinematics), i.e., $\boldsymbol{\varepsilon} = \frac{1}{2}(\boldsymbol{\nabla u} + \boldsymbol{\nabla u}^\intercal)$.

To solve the problem with the finite element method, we look for the weak form of equilibrium and then discretize the equations using vector-valued finite element spaces. In particular, we introduce the vector-valued space of test functions

$$\boldsymbol{\mathcal{V}}_0(\Omega) = \left\{ \boldsymbol{w} : \boldsymbol{w}(\boldsymbol{x}) \in \mathbb{R}^2 \; \forall \boldsymbol{x} \in \Omega, \, \boldsymbol{w}|_{\Gamma^D} = \boldsymbol{0} \right\} \subset \boldsymbol{\mathcal{H}}^1(\Omega), \tag{5}$$

where $\boldsymbol{\mathcal{H}}^1(\Omega) \equiv \left[\mathcal{H}^1(\Omega)\right]^2$ and $\mathcal{H}^1(\Omega)$ denotes the first-order Sobolev function space on Ω.

The variational formulation is: Find $\boldsymbol{u} \in \boldsymbol{\mathcal{U}}$ such that

$$\mathscr{B}(\boldsymbol{u}, \boldsymbol{w}) = \mathscr{L}(\boldsymbol{w}), \qquad \forall \boldsymbol{w} \in \boldsymbol{\mathcal{V}}_0, \tag{6}$$

with bilinear and linear forms defined by

$$\mathscr{B}(\boldsymbol{u}, \boldsymbol{w}) = \int_\Omega \boldsymbol{\nabla w} : \boldsymbol{\sigma} \, \mathrm{d}\Omega, \tag{7}$$

$$\mathscr{L}(\boldsymbol{w}) = \int_\Omega \boldsymbol{w} \cdot \boldsymbol{b} \, \mathrm{d}\Omega + \int_{\Gamma^N} \boldsymbol{w} \cdot \bar{\boldsymbol{t}} \, \mathrm{d}\Gamma, \tag{8}$$

respectively. Note that $\boldsymbol{u}$ is taken from the set

$$\boldsymbol{\mathcal{U}}(\Omega) = \left\{ \boldsymbol{u} : \boldsymbol{u}(\boldsymbol{x}) \in \mathbb{R}^2 \; \forall \boldsymbol{x} \in \Omega, \, \boldsymbol{u}|_{\Gamma^D} = \bar{\boldsymbol{u}} \right\} \subset \boldsymbol{\mathcal{H}}^1. \tag{9}$$

It is common, however, to write $\boldsymbol{u} = \boldsymbol{v} + \tilde{\boldsymbol{u}}$, with $\tilde{\boldsymbol{u}}|_{\Gamma^D} = \bar{\boldsymbol{u}}$, so that $\boldsymbol{v} \in \boldsymbol{\mathcal{V}}_0(\Omega)$. In other words, we seek for the *unknown part* of the displacement field in the same vector-valued function space where test functions are taken from. Taking both $\boldsymbol{v}, \boldsymbol{w} \in \boldsymbol{\mathcal{V}}_0(\Omega)$ is known as the Bubnov-Galerkin formulation, leading to symmetric system matrices [36].

2.1. Discontinuity-enriched finite element discretization

The solution to the variational formulation (6) necessitates a discretization process. Therefore, we first rewrite (6) into:

$$\mathscr{B}\left(\boldsymbol{v}^h, \boldsymbol{w}^h\right) = \mathscr{L}\left(\boldsymbol{w}^h\right) - \mathscr{B}\left(\tilde{\boldsymbol{u}}, \boldsymbol{w}^h\right), \qquad \forall \boldsymbol{w}^h \in \boldsymbol{\mathcal{S}}^h(\Omega), \tag{10}$$

where the test function $\boldsymbol{w}^h$ and the trial solution $\boldsymbol{v}^h$ are taken from the discontinuity-enriched finite element space

$$\boldsymbol{\mathcal{S}}^h(\Omega) = \left\{ \boldsymbol{v}^h(\boldsymbol{x}) = \underbrace{\sum_{i \in \iota_h} \varphi_i(\boldsymbol{x}) \boldsymbol{u}_i}_{\text{standard FEM}} + \underbrace{\overbrace{\sum_{i \in \iota_w} \psi_i(\boldsymbol{x}) \boldsymbol{\alpha}_i}^{\text{weak}} + \overbrace{\sum_{i \in \iota_s} \sum_{1 \le k \le n-1} \chi_{ik}(\boldsymbol{x}) \boldsymbol{\beta}_{ik}}^{\text{strong}}}_{\text{enrichment}}, \; \boldsymbol{u}_i, \boldsymbol{\alpha}_i, \boldsymbol{\beta}_{ik} \in \mathbb{R}^2 \right\}. \tag{11}$$

Here we follow the DE-FEM enrichment scheme for multiple intersecting discontinuities developed by Liu et al. [43] since some cut finite elements can be intersected by multiple cracks—particularly those that contain merging cracks. This approach has been proven effective in resolving the kinematics of branched cracks and polycrystalline microstructures under mechanical and thermal loadings, achieving the same accuracy as standard FEM on fitted meshes [43].

In (11), the standard FEM component is hierarchically augmented with enrichment terms that incorporate the kinematics of weak and strong discontinuities. In the first term, ι_h is the set of all standard FEM nodes, φ_i is the Lagrange shape function of the ith standard node, and $\boldsymbol{u}_i$ are its associated DOFs. The enrichment is composed of two terms. In the weak enrichment, ι_w is the index set of weak nodes, each associated with weak enrichment functions ψ_i and enriched DOFs $\boldsymbol{\alpha}_i$; this term is used to capture the

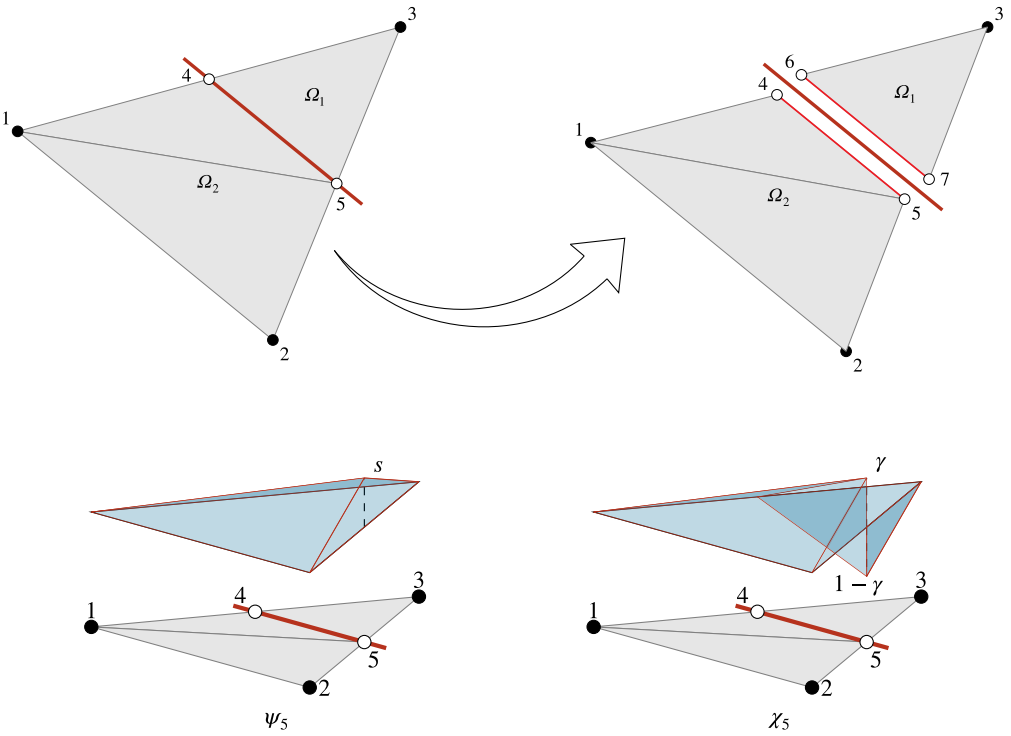

Fig. 2. (top) A triangular element with nodes 1, 2, 3 cut by a single discontinuity in standard FEM. The element is divided into two subdomains Ω_1, Ω_2; (bottom) Enrichment functions for a node along the discontinuity that reproduce the same kinematics. While the weak enrichment function ψ_5 is continuous the strong enrichment χ_5 is discontinuous.

gradient field jump. In the strong enrichment ι_s is the index set of strong nodes, each associated with enrichment functions χ_{ik} and enriched DOFs $\boldsymbol{\beta}_{ik}$. The enrichments χ_{ik} are constructed so as to ensure that $\boldsymbol{\beta}_{ik}$ represents the displacement jump at the location of the enriched node. Since $n-1$ strong enrichments are required by an n-fold junction, $\boldsymbol{\beta}_{ik}, k = \{1, \dots, n-1\}$ therefore represent the jump between contiguous subdomains separated by a crack. Notice also that no junction implies $n = 2$, thus recovering the original DE-FEM formulation [39].

It is worth noting that, for modeling fracture in homogeneous materials, weak enrichments are also required to provide the formulation with enough DOFs so that completely independent kinematic fields are generated at either side of cracks [39].

When dealing with fracture, most finite elements are cut by single discontinuities. We therefore describe first the DE-FEM enrichment functions for a fully cut element, which is schematically shown in Fig. 2. The discontinuity divides the element into two subdomains Ω_1 and Ω_2. In standard FEM we would subdivide these subdomains into elements with duplicated nodes along the discontinuity to capture the displacement jumps (top of Fig. 2). Conversely, in DE-FEM enriched nodes are placed directly along discontinuities, so the original finite element space is augmented hierarchically. Both standard FEM and DE-FEM have an equivalent number of DOFs. This is accomplished in DE-FEM by adding two enrichment nodes on top of each intersection, and each node is associated with a weak enrichment function (C^0-continuous) and a strong enrichment function (C^{-1}-continuous) (bottom of Fig. 2). For node $\boldsymbol{x}_5$, the weak enrichment is

$$\psi_5 = \begin{cases} s\varphi_7(\boldsymbol{x}) & \text{for } \boldsymbol{x} \in \Omega_1, \\ s\varphi_5(\boldsymbol{x}) & \text{for } \boldsymbol{x} \in \Omega_2, \end{cases} \tag{12}$$

where s is a scaling parameter that is used to prevent ill-conditioned stiffness matrices when discontinuities are arbitrarily close to standard nodes [38]. As discontinuities approach standard nodes, the enriched contributions to the stiffness matrix can grow in magnitude disproportionately when compared to those associated with standard FEM nodes. To understand this, consider in Fig. 3 a cut element, where ω denotes the relative distance from the enriched node to standard FEM node 3, measured along the connecting edge. The Jacobian matrix $\boldsymbol{J}_1$ of integration element e_1 is related to that of its is parent element $\boldsymbol{J}$ through $\boldsymbol{J}_1^{-1} \approx \frac{1}{\omega}\boldsymbol{J}^{-1}$, and $\det(\boldsymbol{J}_1) \approx \omega^2 \det(\boldsymbol{J})$ [38]. As a result, the contribution of element e_1 to the local stiffness matrix is of the same order as that of the parent element because terms containing ω balance each other, i.e., $(1/\omega)^2\,\omega^2 = 1$ (recall that in the local stiffness matrix the inverse of the Jacobian matrix appears twice but the determinant only once). However, for integration element e_2, the Jacobian matrix $\boldsymbol{J}_2$ relates to that of its parent element through $\boldsymbol{J}_2^{-1} \approx \frac{1}{\omega}\boldsymbol{J}^{-1}$ and $\det(\boldsymbol{J}_2) \approx \omega \det(\boldsymbol{J})$, leading to an unbounded growth of the enriched contribution to the stiffness matrix as $\omega \to 0$ (since $(1/\omega)^2\,\omega = 1/\omega$). A scaling parameter was proposed to mitigate this issue, which was derived from a simple 1-D analysis [38]. The scaling factor, which is computed as

$$s = \sqrt{2\omega(1-\omega)}, \tag{13}$$

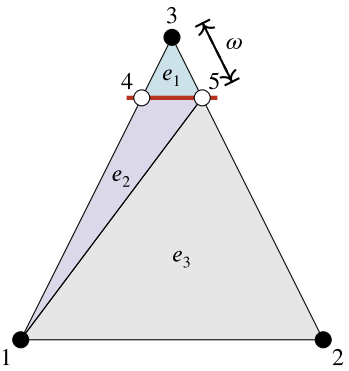

Fig. 3. A triangular element with the discontinuity near one of the nodes.

has also proven to be effective in 2-D and 3-D problems. Therefore, we adopt this scaling parameter for the weak enrichments.

Meanwhile, the strong enrichment function is

$$\chi_5 = \begin{cases} -\gamma\varphi_7(\boldsymbol{x}) & \text{for } \boldsymbol{x} \in \Omega_1, \\ (1-\gamma)\varphi_5(\boldsymbol{x}) & \text{for } \boldsymbol{x} \in \Omega_2, \end{cases} \tag{14}$$

where γ is a parameter that ensures a unity jump at the location of the enriched node, referred to as the strong scaling in our subsequent discussions. Following the original DE-FEM formulation [39], we take γ to be the relative distance from an enriched node to a standard FEM node measured along the edge that connect both nodes—i.e., it is therefore the same as ω. Since it is a relative distance, the length between the nodes is therefore normalized by the edge's length. Notice that since $0 < \gamma < 1$, (14) satisfies a unit jump at the location of the enriched node. Finally, it is important that strong enrichments remain conforming between elements (i.e., there are no gaps); to that end we use the normal to the crack to identify the node to which relative distances are measured. A schematic representation of a strong enrichment function for a node along the single discontinuity is depicted in Fig. 2 (node 5).

A more complex scenario arises when multiple discontinuities intersect within a single element, for which a junction enrichment is required. Without loss of generality, consider the 3-fold junction shown in Fig. 4, where the discontinuities now divide the triangular element into three subdomains Ω_1, Ω_2, and Ω_3. While the standard FEM approach follows the same reasoning above for the fully cut element (top of Fig. 4), in DE-FEM we again construct enrichment functions to hierarchically enhance the FEM shape functions of the uncut element. For a 3-fold junction we therefore have three enrichments (bottom of Fig. 4), where we ensure a unit displacement jump between consecutive subdomains. The weak enrichment is very similar to (12), i.e.,

$$\psi_7 = \begin{cases} s\varphi_7(\boldsymbol{x}) & \text{for } \boldsymbol{x} \in \Omega_1, \\ s\varphi_8(\boldsymbol{x}) & \text{for } \boldsymbol{x} \in \Omega_2, \\ s\varphi_9(\boldsymbol{x}) & \text{for } \boldsymbol{x} \in \Omega_3. \end{cases} \tag{15}$$

The strong enrichment functions are

$$\chi_{71} = \begin{cases} -\gamma\varphi_7(\boldsymbol{x}) & \text{for } \boldsymbol{x} \in \Omega_1, \\ (1-\gamma)\varphi_8(\boldsymbol{x}) & \text{for } \boldsymbol{x} \in \Omega_2, \\ (1-\gamma)\varphi_9(\boldsymbol{x}) & \text{for } \boldsymbol{x} \in \Omega_3, \end{cases} \quad \text{and} \quad \chi_{72} = \begin{cases} 0 & \text{for } \boldsymbol{x} \in \Omega_1, \\ 0 & \text{for } \boldsymbol{x} \in \Omega_2, \\ \varphi_9(\boldsymbol{x}) & \text{for } \boldsymbol{x} \in \Omega_3. \end{cases} \tag{16}$$

Notice that while χ_{71} is built in a similar way to (14), χ_{72} is simply the Lagrange shape function in the third subdomain—which is similar to the approach taken by standard FEM.

The enrichments above are now generalized for an n-fold junction, comprised of a single C^0-continuous weak enrichment

$$\psi_i = s\varphi_i(\boldsymbol{x}) \quad \text{for } \boldsymbol{x} \in \Omega_k, \; k = \{1, \dots, n\}, \tag{17}$$

and $n-1$ discontinuous enrichments with $k = \{2, \dots, n-1\}$

$$\chi_{i1}(\boldsymbol{x}) = \begin{cases} -\gamma_{i1}\varphi_i(\boldsymbol{x}) & \text{for } \boldsymbol{x} \in \Omega_1, \\ (1-\gamma_{i1})\varphi_i(\boldsymbol{x}) & \text{for } \boldsymbol{x} \in \Omega_j, \; j = \{2, \dots, n\}, \end{cases} \tag{18}$$

$$\chi_{ik}(\boldsymbol{x}) = \begin{cases} \varphi_i(\boldsymbol{x}) & \text{for } \boldsymbol{x} \in \cup_{j=k+1}^{n} \Omega_j, \\ 0 & \text{otherwise}, \end{cases} \tag{19}$$

where Ω_k denotes the kth junction's subdomain.

The discretized version of the variational formulation (6) results in a system of linear equations

$$\boldsymbol{K}\boldsymbol{U} = \boldsymbol{F}, \tag{20}$$

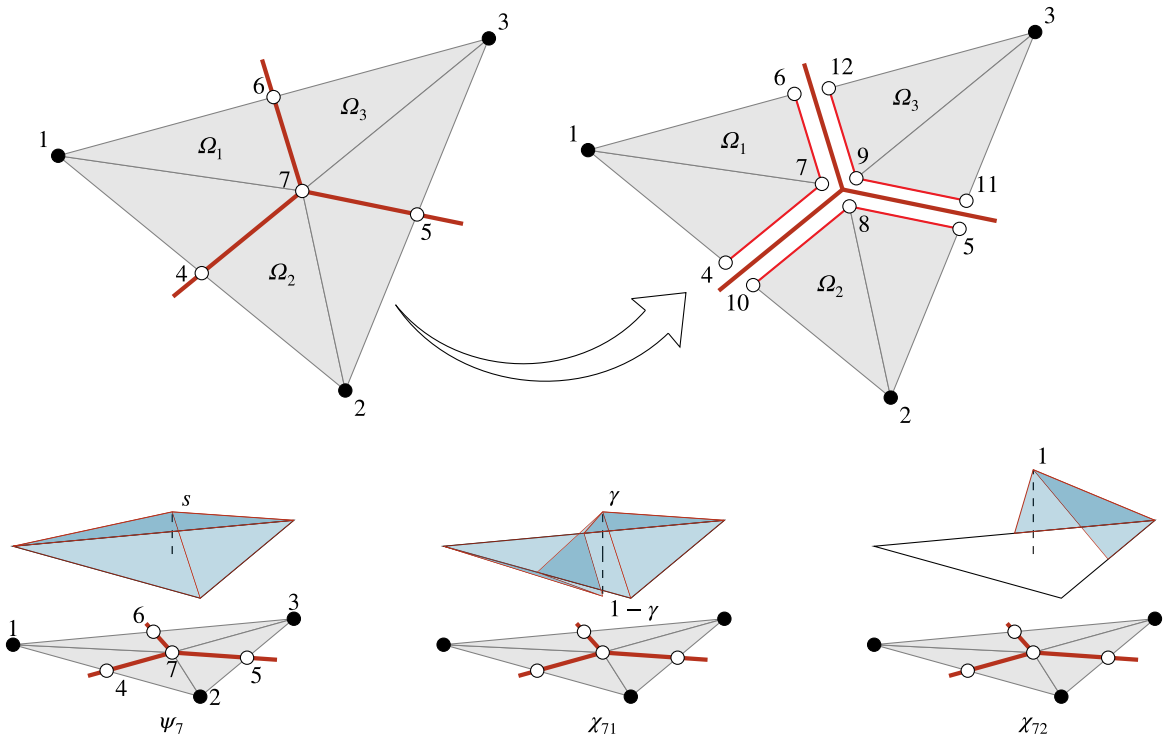

Fig. 4. (top) A triangular element with nodes 1, 2, 3 cut by three discontinuities in standard FEM norm. The element is divided into 3 domains Ω_1, Ω_2, Ω_3. (bottom) Enrichment functions for a 3-fold junction node. ψ_7: The weak enrichment function, χ_{71}: The first strong enrichment function, χ_{72}: The second strong enrichment function.

where $\boldsymbol{K}$ is the global stiffness matrix and $\boldsymbol{F}$ the global force vector. These are built by assembling the local contributions of each finite element. While uncut finite elements follow standard procedures, cut elements deserve some attention. The local stiffness matrix $\boldsymbol{k}_e$ and local force vector $\boldsymbol{f}_e$ at the eth *integration element* are given by

$$\boldsymbol{k}_e = \int_e \boldsymbol{B}^\intercal \boldsymbol{D}\boldsymbol{B}\,\mathrm{d}e \quad \text{and} \quad \boldsymbol{f}_e = \int_e \boldsymbol{\Phi}^\intercal \boldsymbol{b}\,\mathrm{d}e + \int_{\partial e \cap \Gamma^N} \boldsymbol{\Phi}^\intercal \bar{\boldsymbol{t}}\,\mathrm{d}\partial e\,, \tag{21}$$

respectively, where $\boldsymbol{D}$ is the material constitutive matrix, $\boldsymbol{\Phi}$ is the local matrix of shape functions and $\boldsymbol{B}$ is the local strain–displacement matrix. $\boldsymbol{\Phi}$ and $\boldsymbol{B}$ are given, respectively, by

$$\boldsymbol{\Phi} = \begin{bmatrix} \varphi_1 & 0 & \cdots & \psi_1 & 0 & \cdots & \chi_1 & 0 & \cdots \\ 0 & \varphi_1 & \cdots & 0 & \psi_1 & \cdots & 0 & \chi_1 & \cdots \end{bmatrix}, \tag{22}$$

$$\boldsymbol{B} = \begin{bmatrix} \frac{\partial \varphi_1}{dx} & 0 & \cdots & \frac{\partial \psi_1}{dx} & 0 & \cdots & \frac{\partial \chi_1}{dx} & 0 & \cdots \\ 0 & \frac{\partial \varphi_1}{dy} & \cdots & 0 & \frac{\partial \psi_1}{dy} & \cdots & 0 & \frac{\partial \chi_1}{dy} & \cdots \\ \frac{\partial \varphi_1}{dy} & \frac{\partial \varphi_1}{dx} & \cdots & \frac{\partial \psi_1}{dy} & \frac{\partial \psi_1}{dx} & \cdots & \frac{\partial \chi_1}{dy} & \frac{\partial \chi_1}{dx} & \cdots \end{bmatrix}. \tag{23}$$

It is worth noting that the local arrays in (21) are computed using the isoparametric mapping of the master element $\triangle = \left\{ \boldsymbol{\xi} = (\xi, \eta) \in \mathbb{R}^2 \,\middle|\, \xi \geq 0, \eta \geq 0, \xi + \eta \leq 1 \right\}$ for the bulk and $| = \{ \zeta \in \mathbb{R} | \; -1 \leq \zeta \leq 1 \}$ for the line integral as

$$\boldsymbol{k}_e = \int_\triangle \boldsymbol{B}^\intercal \boldsymbol{D}\boldsymbol{B}\, j_\triangle\,\mathrm{d}\boldsymbol{\xi} \quad \text{and} \quad \boldsymbol{f}_e = \int_\triangle \boldsymbol{\phi}^\intercal \boldsymbol{b}\, j_\triangle\,\mathrm{d}\boldsymbol{\xi} + \int_| \boldsymbol{\phi}^\intercal \bar{\boldsymbol{t}}\, j_|\,\mathrm{d}\zeta\,, \tag{24}$$

with $j_\triangle$ and $j_|$ denoting their corresponding Jacobians. For more details on the formulation, the reader is referred to Aragón and Duarte [36, Chapter 5].

In our implementation, cracks are defined explicitly as piece-wise line segments. Cut elements are subdivided into subdomains or integration elements, and enriched nodes are also created. All computational geometry operations are carried out by a geometric engine as discussed elsewhere [50]. A more detailed discussion is deferred to Section 3.

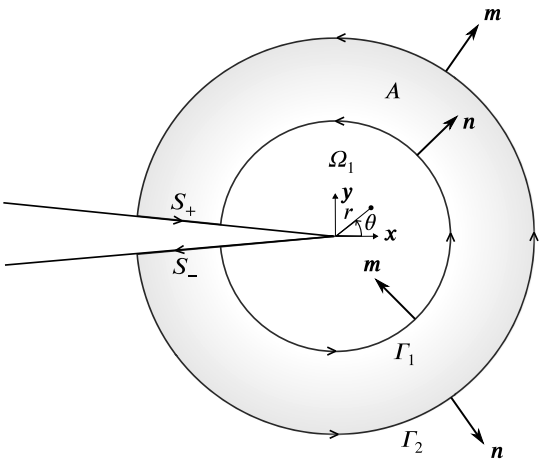

Fig. 5. Notation used for the interaction integral, with normal vector $\boldsymbol{m} = -\boldsymbol{n}$ along Γ_1 and $\boldsymbol{m} = \boldsymbol{n}$ along Γ_2.

2.2. Extraction of stress intensity factors

Stress intensity factors are important parameters employed to quantify the stress level around the crack tip; these are often used to determine when a crack starts propagating and its subsequent propagation direction. Since we focus herein on 2-D problems, we only discuss the mode I (opening) and mode II (in-plane shear) crack loading. In accordance with the LEFM, SIFs are defined as

$$\begin{aligned} K_I &= \lim_{r\to 0} \sqrt{2\pi r}\sigma_{yy} \quad \text{at } \theta = 0, \\ K_{II} &= \lim_{r\to 0} \sqrt{2\pi r}\sigma_{xy} \quad \text{at } \theta = 0, \end{aligned} \tag{25}$$

where r and θ are the polar coordinates of a coordinate system placed at the crack tip that is aligned with the crack orientation (see Fig. 5). SIFs can be evaluated by means of the J-integral [51], which serves as a valuable tool for assessing the energy release rate (i.e., $G = J$); in this work we use the interaction integral proposed by Shih and Asaro [52]:

$$\begin{aligned} I^{(1,2)} &= \int_C \left[\left(\sigma_{ik}^{(1)} \varepsilon_{ik}^{(2)} \delta_{1j} - \sigma_{ij}^{(1)} \frac{\partial u_i^{(2)}}{\partial x_1} - \sigma_{ij}^{(2)} \frac{\partial u_i^{(1)}}{\partial x_1} \right) q_1 m_j \right] \mathrm{d}C \\ &= \int_A \left[\left(-\sigma_{ik}^{(1)} \varepsilon_{ik}^{(2)} \delta_{1j} + \sigma_{ij}^{(1)} \frac{\partial u_i^{(2)}}{\partial x_1} + \sigma_{ij}^{(2)} \frac{\partial u_i^{(1)}}{\partial x_1} \right) \frac{\partial q_1}{\partial x_j} \right] \mathrm{d}A\,, \end{aligned} \tag{26}$$

which computes the interaction between the actual state and an auxiliary state, denoted by superscripts (1) and (2), respectively. The auxiliary terms with superscript (2) are directly obtained from the static asymptotic field, which is given in Appendix A. The conventions for the interaction integral are visually depicted in Fig. 5. In (26), $C = S^+ \cup \Gamma_1 \cup S^- \cup \Gamma_2$ denotes the line contour of the integral, A stands for the integration area bounded by C, q_1 is the weight function with value 1 along Γ_1 and 0 along Γ_2, while m_j is a component of the outward normal vector $\boldsymbol{m}$ to the contour C. In finite element implementations, it is common to employ the domain form of the interaction integral. As this integral is path-independent, the domain and value of the scalar field q_1 is user-defined, as long as its value is 1 along Γ_1 and 0 along Γ_2. Herein we define q_1 for a single crack tip as follows (see Fig. 6): $q_1 = 1$ for all the elements fully enclosed by the circle of radius r, and $q_1 = 0$ on uncut elements elsewhere. Consequently, in cut elements the gradient of q_1 at a particular Gauss point can be calculated by interpolation using the derivatives of shape functions and q_1 values at the nodes of cut elements.

The interaction integral is related to the stress intensity factors for modes I and II (i.e., K_I and K_{II}, respectively) through the formula

$$I^{(1,2)} = \frac{2}{E^*}\left(K_I^{(1)} K_I^{(2)} + K_{II}^{(1)} K_{II}^{(2)} \right) \quad \text{with} \quad E^* = \begin{cases} E & \text{for plane stress,} \\ \frac{E}{1-\nu^2} & \text{for plane strain.} \end{cases} \tag{27}$$

Here E and ν denote Young's modulus and Poisson's ratio, respectively. To obtain the stress intensity factors, we set $K_I^{(2)} = 1, K_{II}^{(2)} = 0$ for the calculation of $K_I^{(1)}$, and $K_I^{(2)} = 0, K_{II}^{(2)} = 1$ for the calculation of $K_{II}^{(1)}$.

Before the crack growth reaches the boundary of the domain, or in multiple crack growth problems, we modify the interaction integral in order to form a closed integration path for the J-integral, taking into account the interaction effects from other cracks and the domain boundary. In light of this, we outline three distinct cases for processing the interaction integral (see Fig. 7), namely where the crack tip approaches the boundary, when it nears another crack, and where closely-spaced crack tips occur. In the case where the crack tip approaches the boundary we simply assign $q_1 = 0$ to nodes along the boundary (see Fig. 7(a)). When a crack tip approaches another crack we set $q_1 = 0$ along the nearby crack (Fig. 7(b)). If the crack that we aim to exclude subdivides the

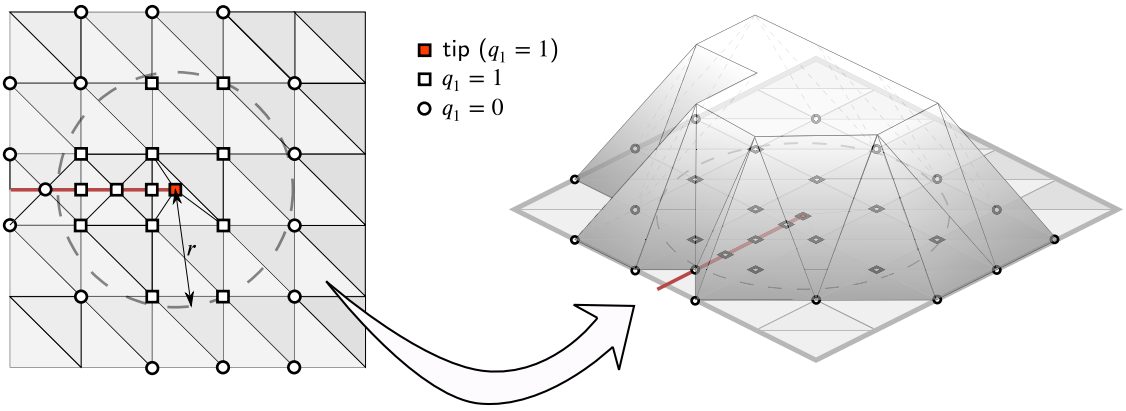

Fig. 6. Magnitude of weight function q_1 for a single crack tip.

computational domain into two, for any node laying in the subdomain that does not contain the crack tip we also set $q_1 = 0$ (see for instance the right-most column of nodes in Fig. 7(b)). Lastly, for closely-spaced crack tips, consider the upper tip of a branch junction shown in Fig. 7(c) as an example; the domain integral of this tip includes the lower branch tip, while the lower crack does not subdivide the computational domain. In such instances, we assign $q_1 = 0$ to all the nodes along the lower crack.

2.3. Criteria for crack growth initiation and propagation direction

As previously mentioned, the modeling of discrete fracture growth relies on external criteria. In this section, we present the criteria employed for crack growth initiation and the determination of the growth direction.

Criterion for crack growth initiation

In our DE-FEM discrete model for crack growth we require a preexisting crack—thus we do not model crack nucleation. To predict the onset of propagation, the Griffith-fracture theory is adopted [46,53], according to which crack growth initiates when the energy release rate G reaches the material-specific critical energy release rate G_c. The energy release rate G is computed as

$$G = \frac{K_I^2 + K_{II}^2}{E^*}, \quad \text{where} \quad E^* = \begin{cases} E & \text{for plane stress,} \\ \frac{E}{1-\nu^2} & \text{for plane strain.} \end{cases} \tag{28}$$

Recall that quantities in (26) and (28) are evaluated at a coordinate system that is aligned with the crack direction. In quasi-static crack growth models, to ensure stable growth under Griffith's criterion, the energy release rate G has to satisfy [54]

$$\left(G - G_c\right) V_c = 0, \tag{29}$$

where V_c is the speed of the crack. This equation is known as the Karush–Kuhn–Tucker (KKT) condition for quasi-static crack growth, which is equivalent to

$$G \leq G_c \quad \text{and} \quad V_c > 0 \quad \text{if} \quad G = G_c. \tag{30}$$

If (30) is not satisfied we have unstable crack growth, which could be modeled with a dynamic analysis [54,55]. In our quasi-static crack growth model, a scaling factor is computed to back-calculate the quantities (forces, displacements, SIFs, etc.) that satisfy (30) at each loading step during propagation. More details about the computer implementation are discussed later in Section 3.

Criteria for crack growth direction

In LEFM, there are three commonly used criteria to determine the crack growth direction:

1. **Maximum circumferential stress criterion (MCS)** According to this criterion, the crack propagates in a direction where the circumferential stress $\sigma_{\theta\theta}$ (expressed in polar coordinates), calculated as

$$\sigma_{\theta\theta} = \sigma_{xx} \sin^2\theta + \sigma_{yy} \cos^2\theta - 2\sigma_{xy} \sin\theta \cos\theta, \tag{31}$$

is maximum. In (31) σ_{xx}, σ_{yy}, and σ_{xy} in Cartesian coordinates take the form of the asymptotic solutions provided in Appendix A. These make use of the SIFs obtained by means of the interaction integral, as explained in Section 2.2. For a given radius r, the circumferential stress is a function of the angle θ alone.
To determine the direction of propagation, we could either compute numerically the angle for which the circumferential stress is maximized, i.e.,

$$\theta_c = \arg\max_{\theta} \sigma_{\theta\theta},$$

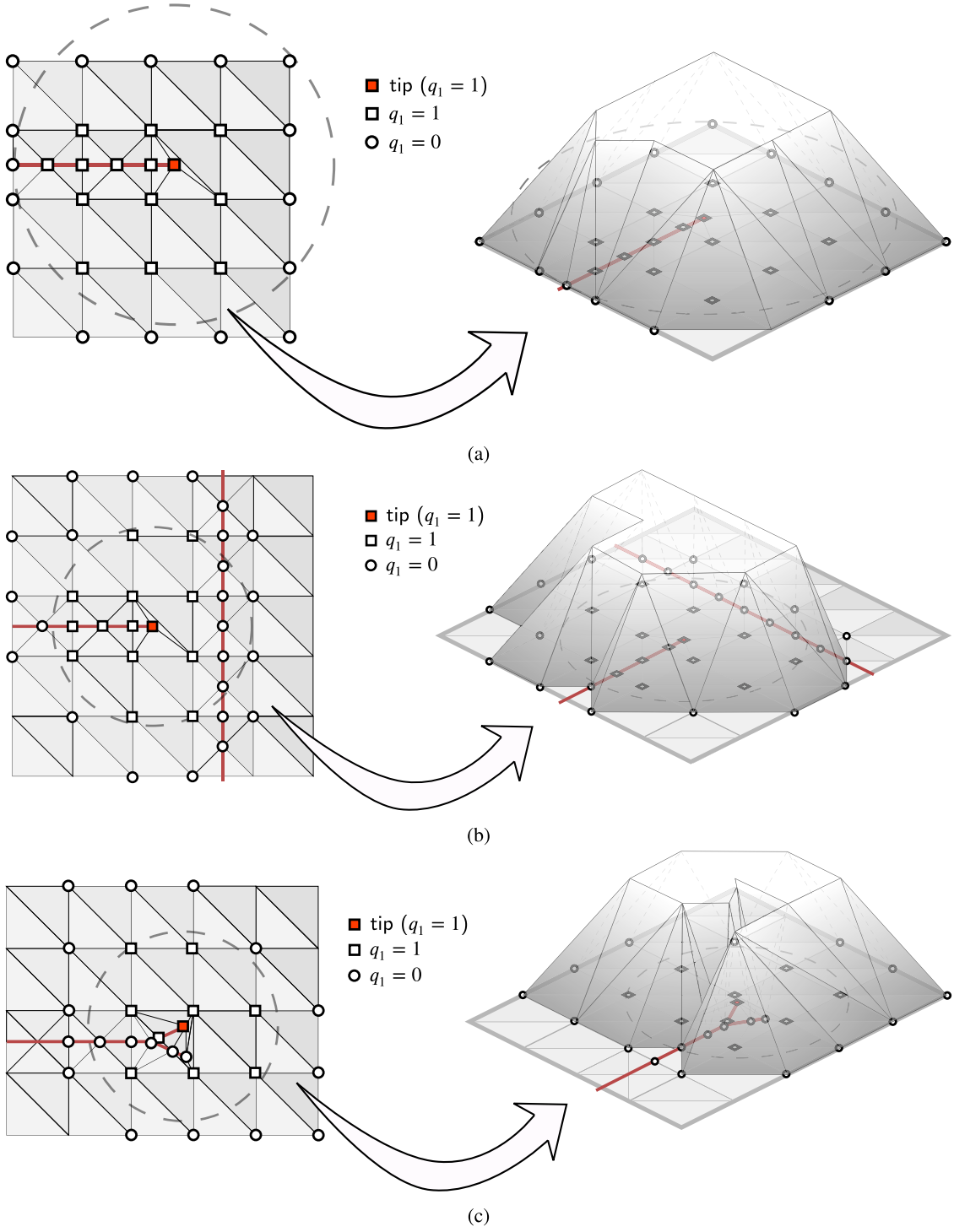

Fig. 7. Weight function q_1 for (a) a tip approaching the boundary of model; (b) a tip approaching another crack; and (c) close crack tips.

which satisfies $\frac{\partial \sigma_{\theta\theta}}{\partial \theta} = 0$, and $\frac{\partial^2 \sigma_{\theta\theta}}{\partial \theta^2} < 0$, or simply obtain it using the commonly used formula [24,25]

$$\theta_c = 2 \arctan\left(\frac{1}{4}\left(\frac{K_I}{K_{II}} - \text{sign}\left(K_{II}\right)\sqrt{8 + \left(\frac{K_I}{K_{II}}\right)^2}\right)\right). \tag{32}$$

The propagation angles obtained from these two approaches are mathematically equivalent in static analysis. Therefore, their computed values should differ only by numerical error. The derivation of (32) is given in Appendix B for completeness.

2. **Minimum strain energy density criterion (MSED)** This criterion states that the crack propagates in the direction where the strain energy density factor S is minimized. Mathematically, this is written as [48]

$$\theta_c = \arg\min_{\theta} S = Wr = \frac{r}{2\mu}\left[\frac{\kappa+1}{8}\left(\sigma_{xx}^2 + \sigma_{yy}^2\right) - \frac{3-\kappa}{4}\sigma_{xx}\sigma_{yy} + \sigma_{xy}^2\right], \tag{33}$$

which satisfies $\frac{\partial S}{\partial \theta} = 0$ and $\frac{\partial^2 S}{\partial \theta^2} > 0$. In (33) W is the strain energy density, $\mu = E/2(1+\nu)$ is the shear modulus, and κ is Kolosov's constant—i.e., $\kappa = 3 - 4\nu$ for plane strain and $\kappa = (3-\nu)/(1+\nu)$ for plane stress. The numerical evaluation of this criterion follows similar steps as those of the maximum circumferential stress criterion. However, there is no closed-form analytical expression for it.

3. **Maximum energy release rate criterion (MERR)** In this criterion, which is based on the analysis of the crack after a small increment, the crack propagates in the direction where the maximum energy is released. By assuming a small crack length increment, the propagation direction is obtained as

$$\theta_c = \arg\max_{\theta} G_\theta = \lim_{r\to 0} \frac{2\pi r}{E^*}\left(\sigma_{\theta\theta}^2 + \sigma_{r\theta}^2\right), \tag{34}$$

which satisfies $\frac{\partial G_\theta}{\partial \theta} = 0$ and $\frac{\partial^2 G_\theta}{\partial \theta^2} < 0$. In (34) G_θ is the energy release rate of the kinked crack [56] and

$$\sigma_{r\theta} = \left(\sigma_{yy} - \sigma_{xx}\right)\sin\theta\cos\theta + \sigma_{xy}\left(\cos^2\theta - \sin^2\theta\right). \tag{35}$$

In this work we use the three criteria to determine whether there are any differences in the results.

3. Computer implementation

Here we discuss implementation details of DE-FEM, emphasizing on the algorithm we used for quasi-static crack growth. The overall structure of the DE-FEM implementation on a displacement-based finite element code is given in Algorithm 1. In the pre-processing stage, we read all necessary data to solve the problem, including the mesh (node and element connectivity arrays), material properties and constitutive laws, cracks' geometry, etc.

We then start the processing stage of the simulation, so we iterate over pseudo-time steps $i \in T$, during which the load increases by a user-defined increment. For simplicity, we assume an initial loading magnitude k and a loading increment Δk. Because the (usually structured) loaded mesh is oblivious to the location of cracks, we then perform operations so that cracks are accounted for in the simulation. This is done by means of a computational geometric engine. We explicitly model discontinuities by means of line segments, so we first detect intersection points between cracks and edges of finite elements in the mesh. Enriched nodes are created at these intersection points, and they are appended to the array used to store the standard FEM node coordinates. Identified cut elements are labeled as parents in an ordered tree data structure; these are further subdivided into children integration elements and added as children to their corresponding parent in the same ordered tree. This entire process is managed by an object-oriented geometric engine that was designed to speedup such tasks [50].

Following the computational geometric operations, we then proceed with assembling and solving the system of linear equations, and thereafter with the algorithm for quasi-static fracture propagation. Therefore, we assemble the global stiffness matrix $\boldsymbol{K}_i$ and the global force vector $\boldsymbol{F}_i$ for the given load magnitude k.

While the assembly procedure is fairly standard in uncut elements, in DE-FEM particular care must be taken while assembling the stiffness matrix and force vector of cut elements. Original mesh elements that are cut are *masked* and not processed further, so only their children elements are extracted from the ordered tree for assembly. The numerical integration of an integration element $e_{\triangle}$ is described in detail in Algorithm 2. The local stiffness matrix and force vector are computed by numerical quadrature, so we iterate over quadrature points $\boldsymbol{\xi}$ with corresponding weights $\boldsymbol{w}$. The number of quadrature points is determined to exactly integrate the functions involved, so for constant material properties we simply use one integration point per element (notice that for triangular elements both parent shape functions and enrichments are linear). At the start of the loop, because enrichment functions are computed with the aid of Lagrange shape functions in integration elements, we first compute these and their derivatives. These are used to compute quantities related to the mapping (the inverse of the Jacobian matrix and its determinant). The global coordinate of the integration point is then calculated using the shape functions and the nodal coordinates of the integration element.

Subsequently, enrichment functions are computed by iterating on a second loop over enriched nodes. We calculate both weak and strong enrichments as described in Section 2.1. The derivatives of the enrichment functions are multiplied by the Jacobian inverse in order to obtain the derivatives with respect to global coordinates. At the end of this second loop, enrichment functions and their derivates are appended to the local shape function matrix and to the strain–displacement matrix, respectively. We note that, before concatenation, the derivatives are rearranged so as to follow Voigt notation. For our 2-D problem, such rearrangement of a weak enrichment ψ_e takes the form:

Algorithm 1 Structure of an enriched finite element code

Input: A file handle f_{in} with input data, which includes mesh data (i.e., a standard FEM mesh $\mathcal{M} = \{\mathcal{N}, \mathcal{E}\}$ composed of a set of nodes $\mathcal{N}$ and a set of elements $\mathcal{E}$), a set of cracks $\mathcal{C}$, boundary conditions $\mathcal{B}$, material properties and constitutive law $\mathcal{D}$, critical energy release rate G_c, initial load magnitude k, LEFM criterion for propagation $\mathcal{L}$, crack increment Δl, tolerance of multiple crack propagation ϵ

Output: For each pseudo-time step, quantities of interest are output to a file (e.g., displacements $\boldsymbol{U}_i$, stresses $\boldsymbol{\sigma}_i$ and strains $\boldsymbol{\epsilon}_i$, energy release rates $\mathcal{G}$, SIFs $\mathcal{K}$, etc.)

function EnrichedFEM
- *– input and initialization stage*
- $\{\mathcal{M}, \mathcal{C}, \mathcal{B}, \mathcal{D}, G_c, k, \ldots\} \leftarrow$ ReadInput(f_{in}) *– get nodes, elements, and BVP data, load magnitude*
- *– loop over pseudo-time steps*
- **for** $i \in T$ **do**
  - $k \leftarrow k + \Delta k$ *– set load level*
  - *– computational geometry operations with cracks that modify the mesh*
  - **for** $c_i \in \mathcal{C}$ **do**
    - $\mathcal{E}_c \leftarrow$ Intersect($\mathcal{E}, c_i$) *– identify cut elements*
    - $\{\mathcal{N}_w, \mathcal{N}_s, \mathcal{E}_q\} \leftarrow$ ProcessCutElement($\mathcal{E}_c, c_i$) *– create enriched nodes and integration elements*
    - $\mathcal{N} \leftarrow \mathcal{N} \cup \mathcal{N}_w \cup \mathcal{N}_s$ *– add weak and strong enriched nodes*
    - $\mathcal{E} \leftarrow (\mathcal{E} \setminus \mathcal{E}_c) \cup \mathcal{E}_q$ *– mask cut elements and add integration elements*
  - *– assemble and solve linear system of equations*
  - $n_D \leftarrow |\mathcal{N}| \times d$ *– get total number of DOFs*
  - $\{\boldsymbol{K}_i, \boldsymbol{F}_i\} \leftarrow \{\boldsymbol{0}_{n_D \times n_D}, \boldsymbol{0}_{n_D \times 1}\}$ *– initialize global arrays*
  - **for** $e \in \mathcal{E}$ **do**
    - $\{\boldsymbol{k}_e, \boldsymbol{f}_e, \mathcal{F}\} \leftarrow$ Quadrature($e, \mathcal{N}, \mathcal{D}, \boldsymbol{b}, n_{\text{GP}}$) *– obtain local arrays and DOFs*
    - $\{\boldsymbol{K}_i, \boldsymbol{F}_i\} \leftarrow$ Assemble($\boldsymbol{K}_i, \boldsymbol{F}_i, \boldsymbol{k}_e, \boldsymbol{f}_e, \mathcal{F}$) *– assemble into global arrays*
  - $\{\boldsymbol{K}_i, \boldsymbol{F}_i\} \leftarrow$ PrescribeBCs($\boldsymbol{K}_i, \boldsymbol{F}_i, \mathcal{B}, k$) *– apply boundary conditions*
  - $\boldsymbol{U}_i \leftarrow \boldsymbol{K}_i^{-1} \boldsymbol{F}_i$ *– solve for displacements*
  - *– post-process solution and output*
  - $\{\boldsymbol{\sigma}_i, \boldsymbol{\epsilon}_i, \ldots\} \leftarrow$ PostProcess($\boldsymbol{U}_i$) *– get stress, strain, and other quantities*
  - *– quasi-static crack growth and output results*
  - CrackGrowth($\boldsymbol{U}_i, \boldsymbol{F}_i, \boldsymbol{\sigma}_i, \boldsymbol{\epsilon}_i, \mathcal{M}, \mathcal{C}, \mathcal{L}, \Delta l, G_c, \epsilon$) *– call stable crack growth*
- **end function**

$$\boldsymbol{\Delta}\left(\boldsymbol{\nabla}_{\boldsymbol{x}}\psi_e\right) = \begin{bmatrix} \frac{\partial \psi_e}{\partial x} & 0 \\ 0 & \frac{\partial \psi_e}{\partial y} \\ \frac{\partial \psi_e}{\partial y} & \frac{\partial \psi_e}{\partial x} \end{bmatrix}.$$

After computing all enrichments, we compute the parent's standard FEM shape functions and derivatives. Given the integration point $\boldsymbol{\xi}_i$ and its corresponding global coordinate $\boldsymbol{x}$, we use the latter to determine the canonical coordinate of the parent element $\boldsymbol{\xi}_p$ by means of an inverse mapping. Notice that in this algorithm there are two mappings involved, that related to the integration element and that of the parent uncut element. Similar operations, as explained earlier for the enrichment function including rearrangement and concatenation, are performed on the standard shape functions and their derivatives. Once the local stiffness matrix and force vector are computed, these are assembled in their corresponding global arrays with the aid of the element freedom table, which maps local DOFs to global DOFs.

The system of linear equations is solved for the displacement vector after prescribing boundary conditions. We then obtain the stress field in a post-processing step, which is needed thereafter for computing LEFM-related quantities. For our quasi-static crack propagation simulation, the final step involves determining the next cracked configuration. Our crack growth algorithm satisfies the stability condition (30) mentioned earlier in Section 2.3. One way to ensure stable propagation is to adjust the load by the load parameter, but this would require solving for equilibrium a second time with the adjusted load [29]. Instead, herein we solve for equilibrium only once and we scale all quantities accordingly [57].

Algorithm 2 Numerical quadrature in integration elements

Input: Integration element $e_\diamondsuit$, node set $\mathcal{N}$, constitutive law $\mathcal{D}$, body force $\boldsymbol{b}$, number of integration points n_{GP}
Output: Local element arrays $\boldsymbol{k}_e$, $\boldsymbol{f}_e$, and corresponding element freedom table $\mathcal{F}$

function QUADRATURE
- $e \leftarrow \text{GETPARENT}\left(e_\diamondsuit\right)$ – *get parent element*
- $\mathcal{F} \leftarrow \text{DOFS}\left(e, e_\diamondsuit\right)$ – *get element freedom table*
- $n \leftarrow |\mathcal{F}|$ – *get total number of local DOFs*
- $\left\{\boldsymbol{k}_e, \boldsymbol{f}_e\right\} \leftarrow \left\{\boldsymbol{0}_{n\times n}, \boldsymbol{0}_{n\times 1}\right\}$ – *initialize local arrays*
- $\left\{\boldsymbol{X}_\diamondsuit, \boldsymbol{X}\right\} \leftarrow \text{GETCOORDINATES}\left(e_\diamondsuit, e\right)$ – *get nodal coordinates of both elements*
- *– loop over integration points*
- $\{\boldsymbol{w}, \boldsymbol{\xi}\} \leftarrow \text{QUADRATURERULE}(n_{\text{GP}})$ – *weights and master coordinates*
- **for** $i \leftarrow \left\{1 \dots n_{\text{GP}}\right\}$ **do**
  - $\boldsymbol{\Phi} \leftarrow \varnothing$ – *shape function matrix*
  - $\boldsymbol{B} \leftarrow \varnothing$ – *strain-displacement matrix*
  - *– operations related to integration element*
  - $\left\{\boldsymbol{\varphi}_\diamondsuit, \boldsymbol{\nabla}_{\boldsymbol{\xi}}\boldsymbol{\varphi}_\diamondsuit\right\} \leftarrow \text{SHAPES}\left(\boldsymbol{\xi}_i, e_\diamondsuit\right)$ – *get Lagrange shape functions/derivatives*
  - $\left\{\boldsymbol{J}_\diamondsuit^{-1}, j_\diamondsuit\right\} \leftarrow \text{JACOBIAN}\left(\boldsymbol{X}_\diamondsuit, \boldsymbol{\nabla}_{\boldsymbol{\xi}}\boldsymbol{\varphi}_\diamondsuit\right)$ – *Jacobian inverse and determinant*
  - $\boldsymbol{x} \leftarrow \boldsymbol{X}_\diamondsuit^{\top}\boldsymbol{\varphi}_\diamondsuit^{\top}$ – *compute global coordinate*
  - *– loop over enriched nodes*
  - **for** $\boldsymbol{x}_e \in e_\diamondsuit \cap \left\{\mathcal{N}_w \cup \mathcal{N}_s\right\}$ **do**
    - **if** $\boldsymbol{x}_e \in \mathcal{N}_w$ **then** – *if weak enriched node*
      - $s \leftarrow \text{WEAKSCALING}\left(\boldsymbol{x}_e, e_\diamondsuit\right)$ – *get weak scaling factor, Eq. (13)*
      - $\left\{f_e, \boldsymbol{\nabla}_{\boldsymbol{\xi}} f_e\right\} \leftarrow \text{WEAK}\left(s, \boldsymbol{\varphi}_\diamondsuit, \boldsymbol{\nabla}_{\boldsymbol{\xi}}\boldsymbol{\varphi}_\diamondsuit\right)$ – *calculate weak enrichments/derivatives*
    - **else if** $\boldsymbol{x}_e \in \mathcal{N}_s$ **then** – *if strong enriched node*
      - $\gamma \leftarrow \text{STRONGSCALING}\left(\boldsymbol{x}_e, e_\diamondsuit\right)$ – *get strong scaling factors*
      - $\left\{f_e, \boldsymbol{\nabla}_{\boldsymbol{\xi}} f_e\right\} \leftarrow \text{STRONG}\left(\gamma, \boldsymbol{\varphi}_\diamondsuit, \boldsymbol{\nabla}_{\boldsymbol{\xi}}\boldsymbol{\varphi}_\diamondsuit\right)$ – *calculate strong enrichments/derivatives*
    - $\boldsymbol{\Phi} \leftarrow \left[\boldsymbol{\Phi} \quad f_e \odot \boldsymbol{I}\right]$ – *concatenate enrichment function*
    - $\boldsymbol{B} \leftarrow \left[\boldsymbol{B} \quad \boldsymbol{\Delta}\left(\boldsymbol{\nabla}_{\boldsymbol{x}} f_e\right)\right]$ – *rearrange and concatenate derivatives*
  - *– operations involving parent element*
  - $\boldsymbol{\xi}_p \leftarrow \text{INVERSEMAPPING}(\boldsymbol{x})$ – *find master coordinate*
  - $\left\{\boldsymbol{\varphi}, \boldsymbol{\nabla}_{\boldsymbol{\xi}}\boldsymbol{\varphi}\right\} \leftarrow \text{SHAPES}\left(\boldsymbol{\xi}_p, e\right)$ – *shape functions/derivatives*
  - $\left\{\boldsymbol{J}^{-1}, j\right\} \leftarrow \text{JACOBIAN}(\boldsymbol{X}, \boldsymbol{\nabla}_{\boldsymbol{\xi}}\boldsymbol{\varphi})$ – *Jacobian inverse and determinant*
  - $\boldsymbol{\nabla}_{\boldsymbol{x}}\boldsymbol{\varphi} \leftarrow \boldsymbol{J}^{-1}\boldsymbol{\nabla}_{\boldsymbol{\xi}}\boldsymbol{\varphi}$ – *derivatives w.r.t. global coordinates*
  - $\boldsymbol{\Phi} \leftarrow \left[\boldsymbol{\Phi} \quad \boldsymbol{\varphi} \odot \boldsymbol{I}\right]$ – *concatenate standard FEM shape functions*
  - $\boldsymbol{B} \leftarrow \left[\boldsymbol{B} \quad \boldsymbol{\Delta}\left(\boldsymbol{\nabla}_{\boldsymbol{x}}\boldsymbol{\varphi}\right)\right]$ – *rearrange and concatenate derivatives*
  - *– add contributions to local arrays*
  - $\boldsymbol{C} \leftarrow \text{CONSTITUTIVE}\left(\boldsymbol{x}, D\right)$ – *get constitutive matrix*
  - $\boldsymbol{k}_e \leftarrow \boldsymbol{k}_e + w_i\, j_\diamondsuit\, \boldsymbol{B}^{\top}\boldsymbol{C}\,\boldsymbol{B}$ – *update stiffness matrix*
  - $\boldsymbol{f}_e \leftarrow \boldsymbol{f}_e + w_i\, j_\diamondsuit\, \boldsymbol{\Phi}^{\top}\boldsymbol{b}$ – *update force vector*
- **return** $\left\{\boldsymbol{k}_e, \boldsymbol{f}_e, \mathcal{F}\right\}$

end function

The pseudo-code for the stable growth of multiple cracks is described in Algorithm 3. Given the set of tips $\mathcal{T}$, we first compute all their SIFs and energy release rates, and we determine thereafter the maximum energy release rate G_i. Cracks propagate once the

Algorithm 3 Algorithm for stable growth of multiple cracks

Input: Solution vector $\boldsymbol{U}_i$, force vector $\boldsymbol{F}_i$, stress field $\boldsymbol{\sigma}_i$, strain field $\boldsymbol{\epsilon}_i$ mesh $\mathcal{M}$, set of cracks C, LEFM criterion for propagation $\mathcal{L}$, crack increment Δl, critical energy release rate G_c, tolerance of multiple crack propagation ϵ

function CrackGrowth
- $\mathcal{T} \leftarrow$ getTips$(\mathcal{M}, C)$ – *get tips*
- $\mathcal{G} \leftarrow \emptyset$ – *initialize set of energy release rates*
- $\mathcal{K} \leftarrow \emptyset$ – *initialize set of SIFs*
- *– compute and store SIFs and energy release rates*
- **for** $t \in \mathcal{T}$ **do** – *loop over tips*
  - $\{K_I, K_{II}\} \leftarrow$ getSIFs$(t, \boldsymbol{\sigma}_i, \mathcal{M})$ – *calculate SIFs for tip t, Eqs. (26)–(27)*
  - $\mathcal{K} \leftarrow \mathcal{K} \bigcup \{K_I, K_{II}\}$ – *store SIFs*
  - $G \leftarrow \frac{K_I^2 + K_{II}^2}{E^*}$ – *compute energy release rate, Eq. (28)*
  - $\mathcal{G} \leftarrow \mathcal{G} \bigcup G$ – *store energy release rate*
- $\mathcal{A} \leftarrow \emptyset$ – *initialize set of active tips*
- $G_i \leftarrow \max(\mathcal{G})$ – *get maximum energy release rate*
- *– propagate cracks and scale quantities if needed*
- **if** $G_i > G_c$ **then** – *check for propagation, see Eq. (30)*
  - $\alpha_i \leftarrow \sqrt{\frac{G_i}{G_c}}$ – *compute scaling factor, Eq. (36)*
  - $\{\boldsymbol{U}_i, \boldsymbol{F}_i, \boldsymbol{\sigma}_i, \boldsymbol{\epsilon}_i\} \leftarrow \left\{\frac{\boldsymbol{U}_i}{\alpha_i}, \frac{\boldsymbol{F}_i}{\alpha_i}, \frac{\boldsymbol{\sigma}_i}{\alpha_i}, \frac{\boldsymbol{\epsilon}_i}{\alpha_i}\right\}$ – *scale quantities of interest for output*
  - **for** $t \in \mathcal{T}$ **do** – *loop over tips*
    - $\{G, K_I, K_{II}\} \leftarrow \left\{\frac{G}{\alpha_i^2}, \frac{K_I}{\alpha_i}, \frac{K_{II}}{\alpha_i}\right\}$ – *scale fracture quantities*
    - **if** $\left|\frac{G - G_c}{G_c}\right| < \epsilon$ **then** – *check if G close to G_c (within tolerance)*
      - $\mathcal{A} \leftarrow \mathcal{A} \bigcup t$ – *add tip to active set*
  - $\Delta l_i \leftarrow \frac{\Delta l}{|\mathcal{A}|}$ – *obtain propagation length for current step*
  - *– update cracks according to growth criteria for the next iteration*
  - **for** $t \in \mathcal{A}$ **do** – *loop over active tips*
    - $\theta_c \leftarrow$ getDirection$(K_I, K_{II}, \mathcal{L})$ – *compute direction, Eq. (32), (33), or (34)*
    - $\boldsymbol{x}_m \leftarrow$ checkMerging$(t, \theta_c, \Delta l_i, C)$ – *find merging point*
    - *– Change fractured configuration*
    - **if** $\boldsymbol{x}_m \neq \emptyset$ **then** – *check if there is a merge*
      - $C \leftarrow$ Merge$(t, \boldsymbol{x}_m, C)$ – *merge cracks*
    - **else**
      - $C \leftarrow$ Propagate$(t, \theta_c, \Delta l_i, C)$ – *propagate cracks*
  - *– output the results to a file*
  - WriteOutput$(\mathcal{M}, \boldsymbol{U}_i, \boldsymbol{F}_i, \boldsymbol{\sigma}_i, \boldsymbol{\epsilon}_i, \mathcal{G}, \mathcal{K}, \ldots)$ – *write results to file*

end function

maximum energy release rate G_i is larger or equal to the critical energy release rate G_c, so at this point we determine whether any crack would propagate. If so, we scale all quantities of interest for output. Because SIFs follow a linear relation with the loading through (25) and energy release rates a quadratic relation through (28), we compute the scaling factor α_i to ensure the stability condition as

$$\alpha_i = \sqrt{\frac{G_i}{G_c}}. \tag{36}$$

We note that (36) is equivalent to Equation (34) in Mukhtar et al. [57], where they also use the same factor to scale the loading so that the calculated energy release rate satisfies Griffith's criterion during propagation. Since the displacement and the force vectors follow a linear relation with the applied loading—under our assumptions of small deformation kinematics, linear elasticity, and proportional loading—their magnitudes are scaled during stable crack growth. Gradient fields such as stress and strain are also scaled for output. As explained earlier, by simply scaling these quantities we get away with solving the system of linear equations only once for every pseudo-time step. This also means that even if we have a displacement-controlled or a load-controlled simulation, snap-back behavior may still occur under certain conditions, as demonstrated in Examples 4.2 and 4.4.

The scaling factor α_i is also used to scale the SIFs and energy release rates of every tip. At this point in the algorithm we need to determine the new cracked configuration, for which we first identify all active propagating tips by checking whether their energy release rates are within a tolerance ϵ of G_i. These tips are added to the set $\mathcal{A}$. The propagation length for each crack tip Δl_i is then distributed equally among them, i.e., $\Delta l_i = \Delta l / |\mathcal{A}|$. Note that the crack increment Δl is a user-defined parameter. For every active tip, the propagation direction θ_c is determined by the selected LEFM criterion $\mathcal{L}$. The geometric engine—which is responsible for carrying out all computational geometry operations [50]—then checks for a merging point $\boldsymbol{x}_m$ along the propagation direction within the pre-defined propagation length Δl_i. If $\boldsymbol{x}_m$ exists, a junction is formed at this point, otherwise a new segment is created along the crack without merging with other cracks. Note that even if the geometry of the cracks in the set C is updated, the mesh data structure is not modified further at this stage. All quantities of interest are then output to a file, and this entire process continues until certain condition is met, e.g., complete failure.

4. Numerical examples

In this section we demonstrate DE-FEM's capability for quasi-static crack propagation with a few 2-D examples that are borrowed from the literature. DE-FEM results are then validated with experimental results, and compared to those obtained by other models.

4.1. Compact tension (CT) specimen

In this example we study a compact tension (CT) specimen subjected to tensile loading and its modified version, whereby the crack is subjected to mixed-mode loading. We compare our results with the experimental study conducted by Pham et al. [58] and with the subsequent X/GFEM study by Mukhtar et al. [57]. Fig. 8 shows a schematic representation, together with a finite element discretization for both specimens. For the standard CT specimen we consider an initial sharp crack length $a_0 = 2.74\,\text{mm}$, while the modified specimen has an additional hole and extends the initial sharp crack length to $a_0 = 13.47\,\text{mm}$.

In the original experimental setup, a testing machine was used to apply a monotonically increasing opening displacement vertically at a loading rate of $4 \times 10^{-4}\,\text{mm/s}$. Digital image correction (DIC) was employed to track both the crack opening displacement (COD) along the loading line and the location of the crack front.

We note that the original specimen had a thickness of $3\,\text{mm}$, and therefore we adopt plane stress condition for our analysis. We replicate the experimental setting in our quasi-static analysis with a discretization with mesh size $h_1 = 1\,\text{mm}$. We prescribe a vertical displacement at points a and b in the figure with a constant increment of $\Delta u_y = 0.1\,\text{mm}$, while constraining the horizontal movement. Points c and d in the figure along the loading line are used to measure the COD, which is the cumulative absolute vertical displacements at these points; this quantity is widely used in evaluating the fracture behavior [59]. Polymethylmethacrylate (PMMA) was used in this test, which has a Young's modulus $E = 2.98\,\text{GPa}$, Poisson's ratio $\nu = 0.35$, and critical energy release rate $G_c = 285\,\text{N/m}$. We let the crack propagate with an increment $\Delta l = 0.5\,\text{mm}$ at every propagation step, adjusting it to $0.05\,\text{mm}$ when $K_{II}/K_I > 0.01$.

The reaction force and the crack length, the latter defined as the sum of the initial length and the propagating crack, are plotted in Fig. 9 as a function of COD. As apparent from the figure, we see both DE-FEM and X/GFEM models fit well with the experimental results obtained by Pham et al. [58]. It is worth noting that the X/GFEM result actually uses a 3-D finite element discretization. Yet, the results for both models fall on top of one another for most of the range, with slight differences at the trailing end of the simulation. The DE-FEM curve reaches a peak reaction force of $43.2\,\text{kN}$ at a COD of $0.16\,\text{mm}$.

The results for the modified CT specimen are summarized in Fig. 10(a). The reaction-COD curves exhibit patterns akin to those of the original CT specimen. However, both X/GFEM and DE-FEM models show abrupt softening at the point of crack growth, which is due to the brittle fracture model—i.e., Eq. (29) is highly nonlinear. In contrast, the mild ductility of the experimental specimen contributes to its smooth development during the initial crack formation and a slightly lower critical energy release rate. The DE-FEM curve reaches a peak reaction force of $22.9\,\text{kN}$ at a COD of $0.25\,\text{mm}$. The smaller value of the reaction at the moment of crack growth is due mostly to the larger notch as compared to the standard CT specimen. We note that our assumption of fixed loading points a and b in our models does not fully correspond to the actual experiment, where the loading pins change their location along their corresponding circle perimeter as the specimen is deformed. Our over-constrained boundary condition may then contribute to some of the discrepancies observed.

In addition to the differences observed at the moment of crack growth, the behavior during crack propagation is also different. Regarding the differences between DE-FEM and X/GFEM models, we note once again that while we use a 2-D model under plane stress conditions, X/GFEM uses a 3-D model with a thickness of $3\,\text{mm}$. This leads to a lower energy release rate at the crack tip as compared to the 3-D model. We also note that the zigzag observed on the DE-FEM curve towards the end of the simulation is caused by the limited accuracy in evaluating SIFs with a coarse linear finite element mesh. To examine the influence of the mesh resolution we fix the increment length to $\Delta l = 0.25\,\text{mm}$ and progressively refine the mesh to half and a quarter of the original mesh size h_1.

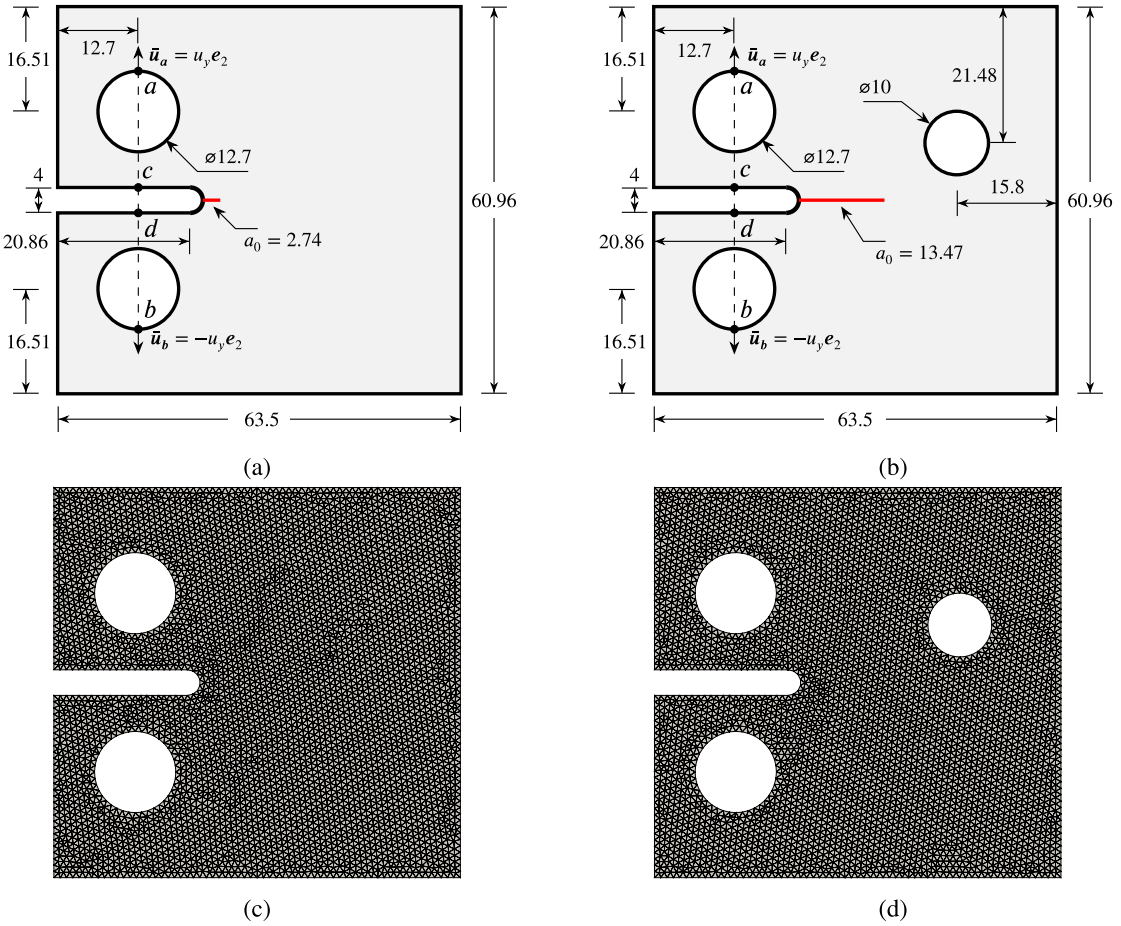

Fig. 8. Schematic of the CT specimen (a) and its modified version (c), together with their corresponding finite element discretizations (b, d). Dimensions are given in mm.

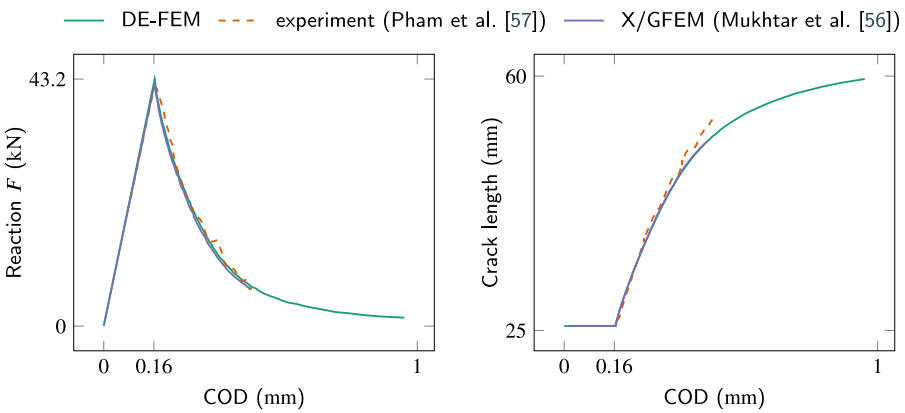

Fig. 9. Results for the original CT specimen under tensile loading, including the reaction-COD (left) and crack length-COD (right).

Note that the increment length is different from that used earlier to get the results of Fig. 10(a) (i.e., 0.5 mm and adjusted to 0.05 mm when $K_{II}/K_I > 0.01$). Fig. 10(b) shows that refining the mesh significantly reduces these oscillations. The inaccurate evaluation of SIFs can lead to jumps in both the energy release rate and the propagation direction. The scaling algorithm in Section 3 in turn leads to the oscillations in reaction-COD curve, particularly under mixed-mode loading. This oscillatory behavior does not appear in the X/GFEM curve [57], likely due to the use of a more accurate quadratic approximation. We also observe that the stiffness of

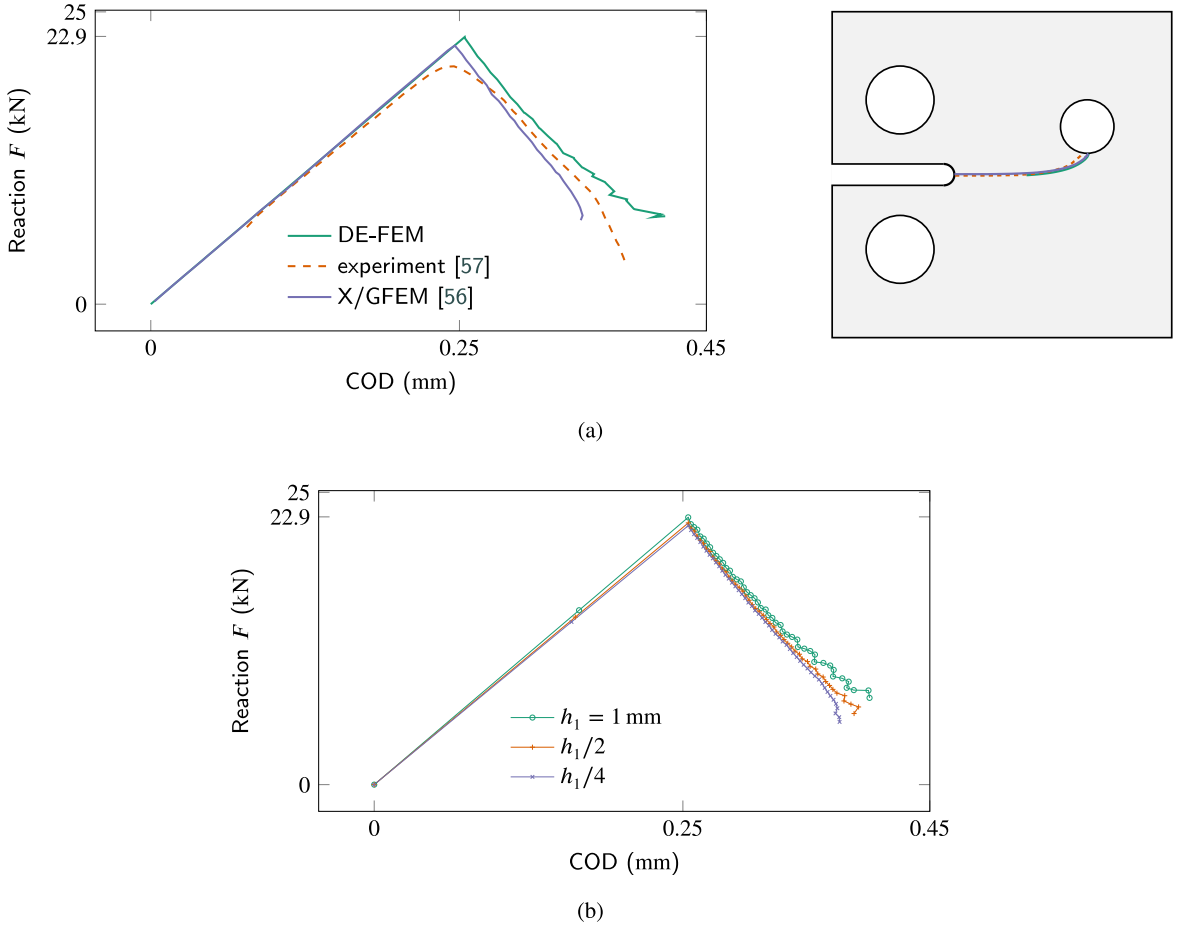

Fig. 10. (a) Results for the modified CT specimen are the reaction-COD (left) and the crack path under mixed-mode loading (right); (b) Effect of mesh resolution on the results for the modified CT specimen. The results show the reaction force F (kN) as a function of COD (mm) for a fixed crack increment length of $\Delta l = 0.25$ mm and increasingly smaller mesh sizes.

the linear part of the curve increases with the mesh size. We note that linear finite elements are not adequate for bending behavior as they undergo shear locking. As the mesh is refined, the reaction force exhibits a steep drop as the crack tip approaches the hole. This behavior aligns well with the trends observed in both the X/GFEM and experiment curves.

4.2. Asymmetric notched three-point bending test

In this example we investigate the asymmetric notched three-point bending test, which is shown schematically in Fig. 11(a). We prescribe the displacement $\bar{u}$ at the middle of the top edge, with an increment in the vertical direction of $\Delta\bar{u} = 0.02$ mm before crack growth initiates. Experiments on this test were carried out by Ingraffea and Grigoriu [60] and have been used to validate different numerical models, including FEM [61], X/GFEM [57,62], phase-field [11,15,18,63], and the thick level-set [64].

We consider a Young's modulus $E = 20.8$ GPa, Poisson's ratio $\nu = 0.3$, and a critical energy release rate $G_c = 1000$ N/m. A plane stress condition is assumed for this test. Due to the presence of holes and asymmetric notch, there is a complex mixed-mode loading at the crack tip throughout crack propagation, leading to the formation of a curvilinear crack trajectory. To accurately capture the crack path, we also reduce the crack length increment $\Delta l = 2$ mm to $\Delta l = 0.2$ mm when the ratio $K_{II}/K_I > 0.01$. The mesh size h chosen for this test is 10 mm. Two different discretizations for this problem are shown in Figs. 11(b) and 11(c). While the former uses a uniform mesh, the latter refines the mesh size within the area containing holes for a more accurate prediction of the crack path.

The results for this example are summarized in Fig. 12, where snap-back behavior is observed. This is because even if the prescribed displacement is monotonically increased during the simulation (i.e., displacement-controlled simulation), the final displacement and force vectors are scaled to capture the actual fields during stable crack propagation, as mentioned in Section 3. The load–displacement curve shows that both discretizations have similar behavior, with a slightly lower value of the reaction force (2.21 kN) and corresponding critical displacement (0.79 mm) at the moment of crack propagation for the refined mesh, compared

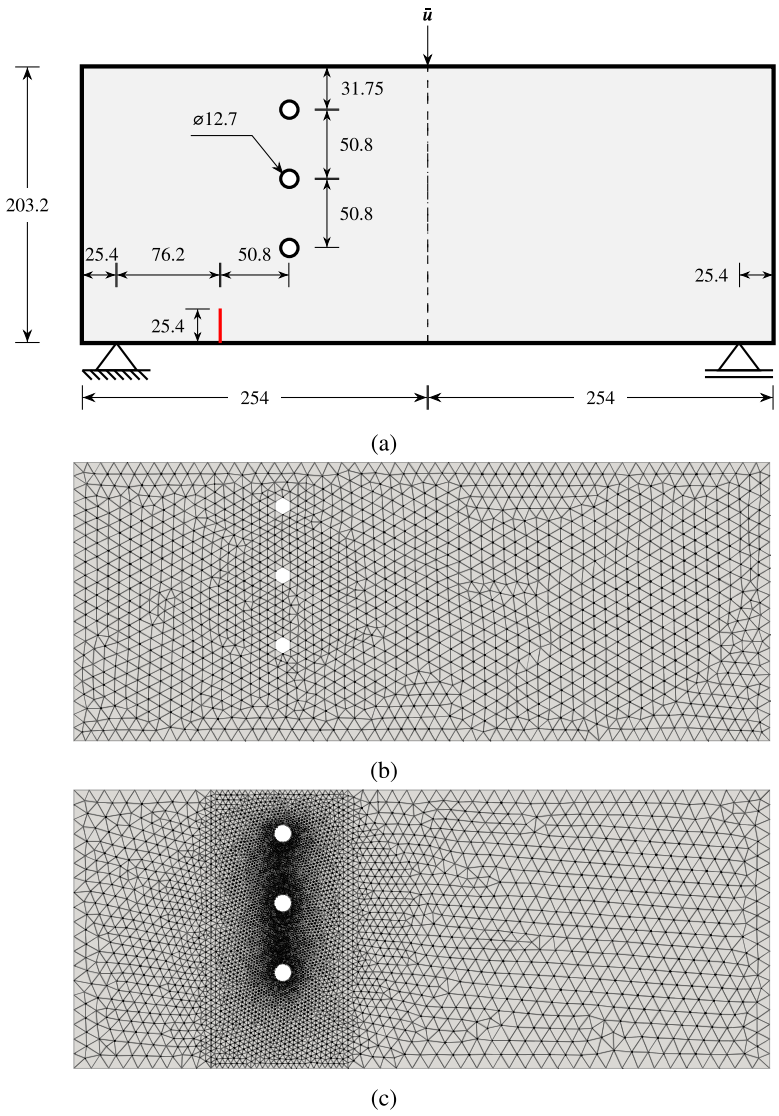

Fig. 11. (a) Schematic of asymmetric bending test; units are given in mm. (b) Regular finite element mesh; and (c) Refined mesh along propagation path.

with the regular mesh (2.28 kN and 0.82 mm). The load–displacement curves closely resemble those obtained by the thick level set model [64]. The final configurations with the circumferential stress criterion for both discretizations are shown in Fig. 12(b). Both discretizations display similar final configurations. Notably, as shown in Fig. 12(c), the crack trajectories successfully reproduce a path obtained experimentally [60] and a path obtained by FEM [61]; this agreement persists regardless of the propagation criterion used, i.e., all criteria used to determine the propagation direction introduced in Section 2.3 reproduce the same path (see Fig. 12(c)).

4.3. Stress intensity factor verification under crack shielding and amplification effects

The previous two examples validated the framework for a single propagating crack. In this example we verify the calculation of SIFs considering multiple cracks. The accurate evaluation of SIFs, taking into account the intricate interaction effects among cracks, has been a challenging topic in discrete crack modeling. Several attempts have been made to improve the precision in the evaluation of SIFs in the presence of closely positioned microcracks. For instance, multiscale X/GFEM [30,31] has been used, whereby SIFs are extracted by the interaction integral method and the cut-off function method. Similarly to the interaction integral, the cut-off function method also extracts SIFs by calculating integrals. However, it avoids the use of derivatives of the displacement field, and reaches high accuracy and convergence rate. We refer to [65–67] for the detailed introduction of the cut-off function method and its applications in *p*-FEM and X/GFEM. In our work we adopt the former for computing SIFs and subsequently verify them while considering crack shielding and amplification effects from closely located microcracks.

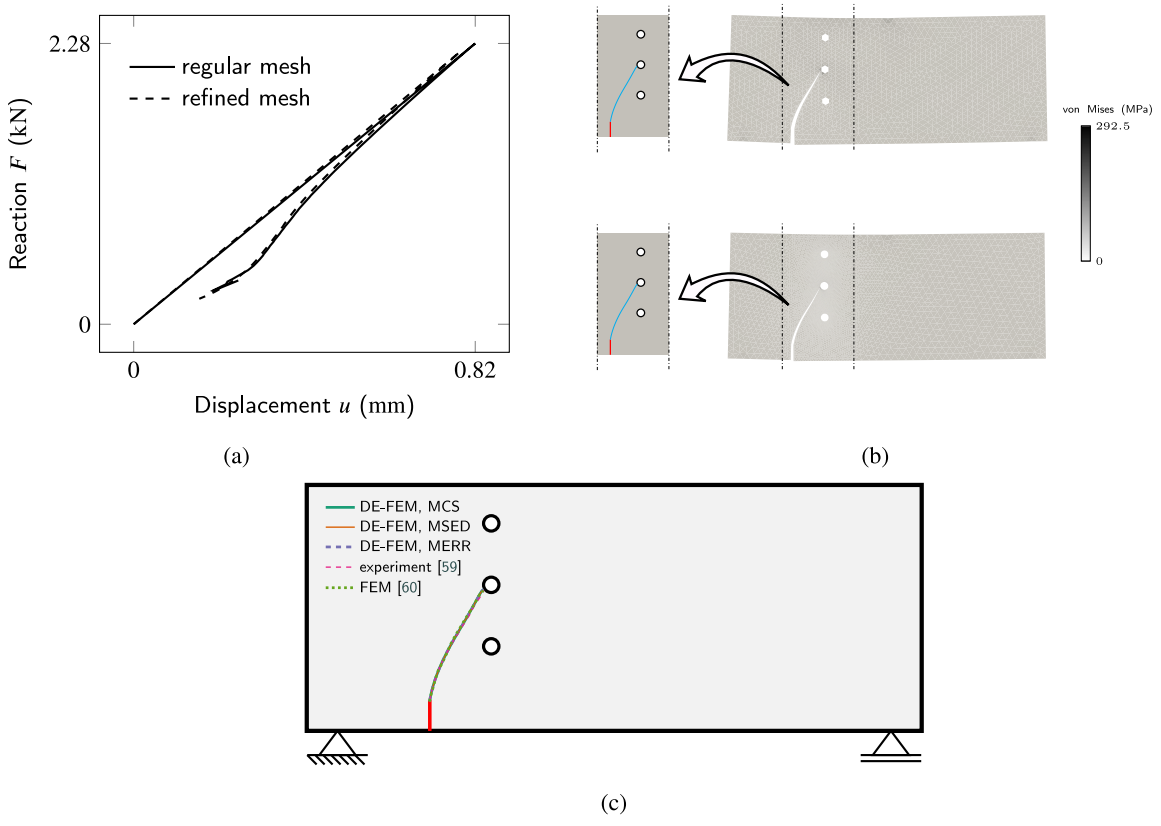

Fig. 12. (a) Load–displacement curves for the asymmetric notched three point bending test; (b) Final configurations for a regular (top) and refined (bottom) meshes; and (c) Crack paths for different crack growth direction criteria.

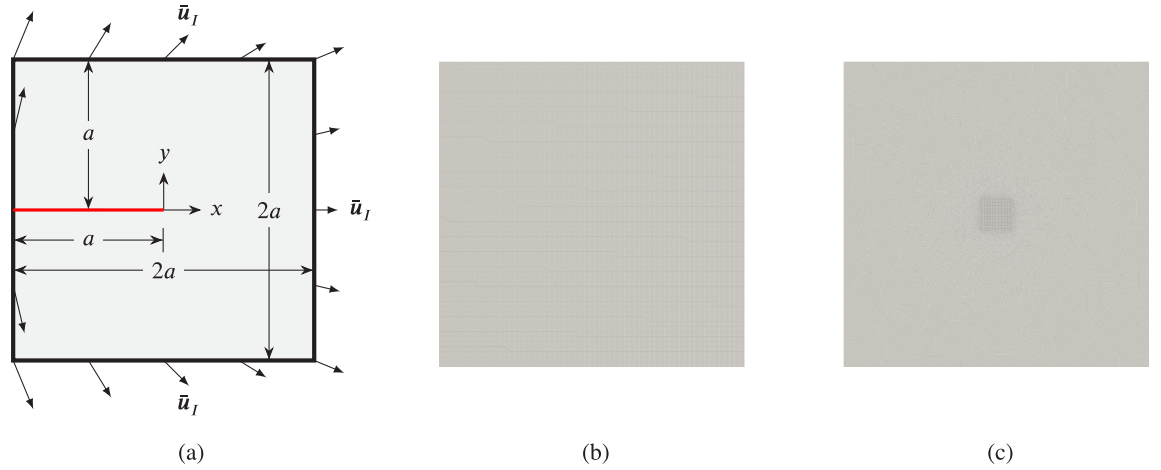

Fig. 13. An edge-notched plate subjected to mode I loading, thereby we prescribe an asymptotic displacement field $\bar{\boldsymbol{u}}_I$; (b, c) Finite element meshes used for the verification of crack shielding and amplification effects: (b) structured; and (c) unstructured refined mesh.

We consider again an edge-notched plate (see Fig. 13(a)) with Young's modulus $E = 1$ and Poisson's ratio $\nu = 0$, similarly to Ref. [31]. We prescribe a mode I asymptotic displacement field $\bar{\boldsymbol{u}}_I$ (given in Appendix A) to the entire boundary of the plate, such that $K_I = 1.0$ in the absence of microcracks. Throughout our subsequent studies, the user-defined radius of the interaction integral used to extract SIFs is denoted as r.

For the numerical solution using DE-FEM we adopt two different mesh configurations: A regular structured mesh (Fig. 14(a)) and an unstructured mesh within refined the area encompassing the microcracks (Fig. 13(c)). The latter was generated by defining

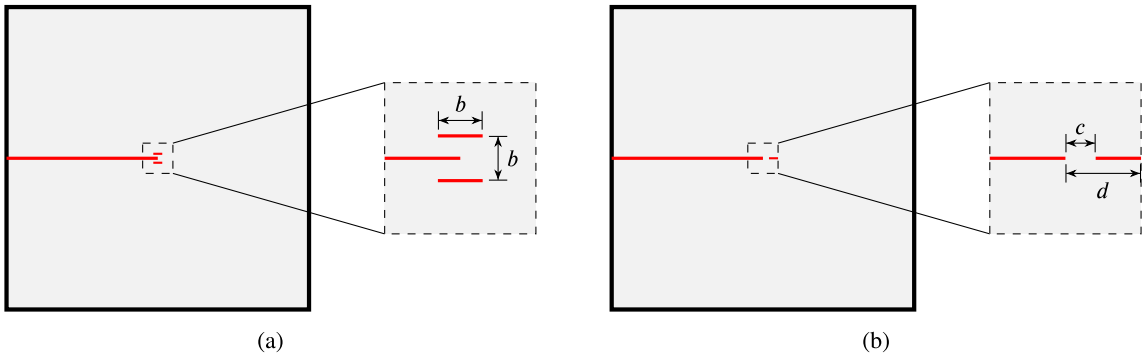

Fig. 14. (a) Shielding configuration; and (b) Amplification configuration.

Table 1
Mode I SIFs of the notch under shielding effects.

b	Reference	Mesh density	K_I^a	K_I^p
$\frac{4}{135}$	Structured mesh	61×61	1.0091	0.9234
		91×91	1.0058	0.813
		121×121	1.0045	0.7836
	Refined mesh	41×41	1.0021	0.6881
		51×51	1.0018	0.6755
		61×61	1.0016	0.6653
	hp-GFEM [31]	–	0.9985	0.6816
	Multiscale XFEM [30]	–	–	0.683
$\frac{4}{27}$	Structured mesh	61×61	1.0091	0.6766
		91×91	1.0058	0.6619
		121×121	1.0045	0.6560
	Refined mesh	41×41	1.0021	0.6370
		51×51	1.0018	0.6370
		61×61	1.0016	0.6362
	Multiscale XFEM [30]	–	–	0.648

a structured mesh within the refined square with dimensions $0.2a$, and using Delaunay triangulation outside of this region. Since the mesh size outside of the refined region has little influence on the resulting SIFs, we simply define the mesh size along the outer boundary as $h = 2a/21$ (i.e., 21 elements per outer edge).

We first examine crack shielding, whereby we position the macrocrack between two horizontal parallel microcracks, as shown in Fig. 14. b represents both the spacing between two microcracks and their lengths. Because no analytical solution is available for the SIFs under shielding effects, we compare our solutions with those found in the literature [30,31]. This comparison is summarized in Table 1 for the two types of discretizations in Fig. 13 and for different mesh sizes within the refined region. To distinguish between results obtained in the absence of microcracks and results obtained in the presence of microcracks, we label the former with a superscript a and the latter with a superscript p. Only the mode I SIFs at the tip of the notch (macrocrack) is evaluated in the crack shielding case. We fix the radius of the interaction integral to $r = 0.1$, ensuring it either encloses or intersects the microcracks.

Examining the data in Table 1, we observe that the evaluated SIFs exhibit clear shielding effects from the microcracks and they tend to converge to the reference values while refining the mesh size. Noteworthy, the results obtained with the structured mesh exhibit substantial deviations from the reference values, when the microcrack size is relatively small (i.e., for $b = 4/135$ we have $K_I^p = 0.7836$ for the finest structured mesh). In comparison, when the microcrack size increases to $b = 4/27$, the error diminishes significantly.

We now turn to the case of crack amplification, whereby a single microcrack is aligned with the notch as shown in Fig. 14(b). c and d are the distances from the microcrack tips to the macrocrack tip. For this case there exists an analytical solution for the SIFs under amplification effect [68,69], and numerical results from X/GFEM have also been reported [31,70]. A comparative summary of these results is presented in Table 2, where SIFs obtained from DE-FEM are extracted by the interaction integral with radius $r = 0.06$. The results show clear amplification effects caused by the microcrack. Even the coarse structured mesh approximates SIFs accurately at the tip of the macrocrack ($x = 0$). Additionally, increasing the size of the microcrack while maintaining the ratio c/d reduces SIFs at the macrocrack. The analytical solution [68,69] suggests that SIFs at these tips are only dependent on the ratio c/d. However, the numerically obtained values change with varying microcrack sizes.

We note that the error obtained with a structured mesh significantly decreases when the microcrack size and the distance between crack tips increase, while keeping the number of elements in the structured mesh constant. This is because when the crack size is relatively small and the crack tips are in close proximity, a finer mesh is necessary to approximate the stress fields accurately.

Table 2
Mode I SIFs for every tip under amplification effects.

c/d	c	d	Reference	Mesh density	$K_I^{(x=0)}$	$K_I^{(x=c)}$	$K_I^{(x=d)}$
	–	–	Analytical [68,69]	–	1.1675	0.8053	0.5343
0.2	0.02	0.1	Structured mesh	61×61	1.0785	0.6593	0.4600
				91×91	1.0861	0.6942	0.4749
				121×121	1.0986	0.7170	0.4852
			Refined mesh	41×41	1.1306	0.7689	0.5119
				51×51	1.1346	0.7738	0.5149
				61×61	1.1375	0.7773	0.5169
			hp-GFEM [31]	–	1.1874	0.8162	0.5457
	0.05	0.25	Structured mesh	61×61	1.0986	0.7362	0.4804
				91×91	1.1069	0.7437	0.4940
				121×121	1.1092	0.7515	0.4965
			Refined mesh	41×41	1.1230	0.7630	0.5136
				51×51	1.1245	0.7645	0.5146
				61×61	1.1245	0.7647	0.5166
			XFEM [70]	–	1.1236	–	–

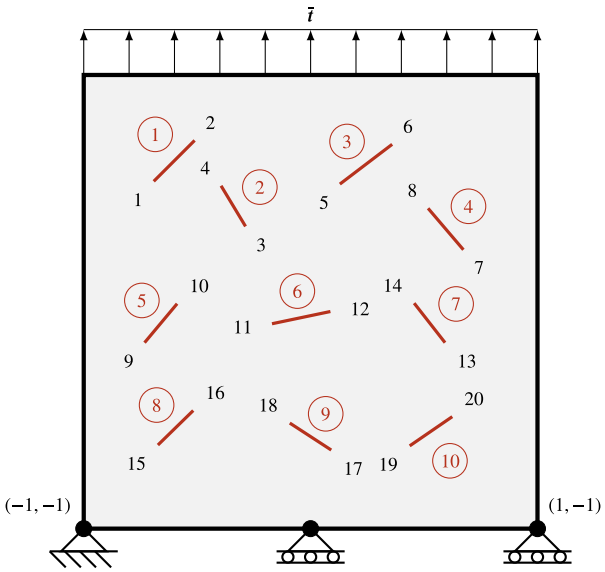

Fig. 15. Schematic of the specimen with randomly distributed defects.

4.4. Multiple crack propagation

In brittle materials such as glass and sandstone the coalescence of cracks is commonly observed. In this study we seek to assess the applicability of DE-FEM in modeling the complex interactions and propagations among multiple cracks. We thus investigate the propagation of randomly distributed defects within a square specimen with side length $a = 2\,\text{mm}$. The geometry of the specimen and the boundary conditions are depicted in Fig. 15. The coordinates of the cracks are provided in Appendix C, mirroring other works [29,32]. Plane strain condition is assumed and we use sandstone material properties, i.e., density $\rho = 2650\,\text{kg/m}^3$, Young's modulus $E = 35\,\text{GPa}$, Poisson's ratio $\nu = 0.3$, and critical energy release rate $G_c = 16.64\,\text{N/m}$. Regarding boundary conditions, the plate is simply supported as shown, and a uniform traction is applied at the top edge. The magnitude of the traction is incremented by $\Delta\bar{t} = 10\,\text{MPa}$ in all time steps, and we scale the output quantities during all propagation steps (see Algorithm 3). Since the different criteria to determine crack propagation direction yielded similar crack paths in Section 4.2, here we choose the maximum circumferential stress criterion.

To obtain the solution to this problem it is imperative to consider the interaction effects among cracks. As discussed in Section 4.3, a fine mesh is required when contemplating the interaction effects from surrounding microcracks. However, given the comparatively large sizes of the distributed cracks in our problem, here we use a structured mesh defined over a 61×61 grid; we assume this mesh will accurately capture the fracture behavior without further mesh refinement. The user-defined crack increment is set to $\Delta l = 0.02\,\text{mm}$. To determine the set of active cracks and allow for their simultaneous propagation in a single step, as outlined in Algorithm 3, here we adopt a tolerance value $\epsilon = G_c/100$.

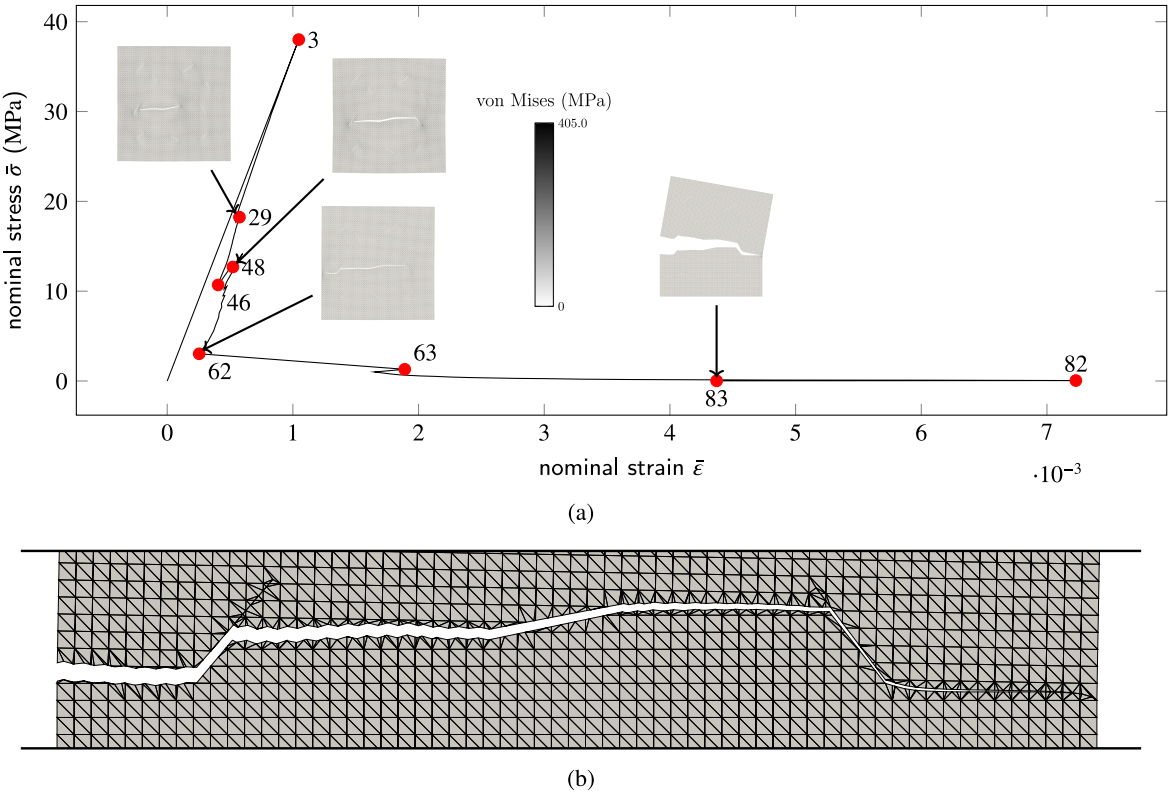

Fig. 16. (a) Nominal stress–strain curve with fractured configurations at steps 29, 48, 62, and 83; and (b) Magnified crack path at step 83.

Fig. 16 shows the nominal stress $\bar{\sigma}$ as a function of nominal strain $\bar{\varepsilon}$ for this problem, which are calculated as

$$\bar{\sigma} = \bar{t}, \qquad \bar{\varepsilon} = \frac{\bar{u}}{a}, \tag{37}$$

where $\bar{t}$ is the magnitude of the applied traction and $\bar{u}$ the average displacement of all nodes along the top edge.

The simulation was carried out until complete fracture in 83 steps (see deformed configurations in the figure at steps 29, 48, 62, and 83). Before any crack propagation, the behavior is linear. The fracture of the specimen starts with the propagation of tip 11 (crack ⑥) towards the left at step 3, where the curve shows a noticeable snap-back behavior. During its propagation, tip 12 also participates intermittently (due to the tolerance ϵ) in several steps. The onset of continuous growth of tip 12 at step 29 introduces a slight deviation in the curve's trajectory. Prior to tip 11 merging with crack ⑤ , it pauses at step 29, at which point tip 12 starts its continuous rightward growth. The strain-stress curve before step 46 experiences a smooth transition, which is attributed to the relatively close energy release rates between tips 11 and 12. At step 46 tip 12 merges with crack ⑦ , followed with the connection between tip 11 and crack ⑤ at step 48. With the merge of tip 11 with crack ⑤ , the stress jumps to control the stable growth as described in Algorithm 3, when a new tip 9 initiates its propagation. The formation of these two junctions corresponds to oscillations in the strain-stress curve. After that, tip 9 grows to the left until reaching the left edge at step 62, showing a significant reduction in strength. Finally, tip 13 propagates to the right and reaches the right edge at step 83. The magnified crack path at the final step 83 is shown in Fig. 16(b), where the zigzag pattern along the crack path is observed. The zigzag is attributed to the inaccurate evaluation of SIFs, which is the same cause of the oscillations discussed in Section 4.1.

5. Summary and conclusions

In this paper we introduced the Discontinuity-Enriched Finite Element Method (DE-FEM) for modeling quasi-static fracture growth in brittle materials. By making use of the recently proposed junction enrichments [43] and the interaction integrals that account for the interplay among cracks, DE-FEM effectively handles the complex interactions encountered by multiple propagating cracks.

Through several examples, we verified the methodology by comparing our results to other discrete models (namely standard FEM and X/GFEM), and we validated our results with experiments. With the first example we studied both a compact tension (CT) specimen under mode I loading and its modification under mixed-mode loading. Load–displacement and crack length-displacement curves agree well with the experimental results and with X/GFEM results obtained using a 3-D model. For the modified CT specimen,

however, DE-FEM showed some discrepancies in propagation initiation time and fracture behavior. We attribute the discrepancy in propagation initiation time between the experiments and DE-FEM to the brittle model assumption. Additionally, the plane stress assumption contributes to the differences in propagation initiation time and fracture behavior observed during propagation between the 2-D DE-FEM model and the 3-D X/GFEM model. In the second example we studied an asymmetric notched three-point bending test, where we were able to reproduce crack paths and load–displacement curves similar to those observed in other models [61,64] and experimental tests [60], and regardless of the mesh size and the LEFM criteria applied.

To assess the accuracy of DE-FEM in handling complex crack configurations, stress intensity factors were computed considering crack shielding and amplification effects. The results indicated that DE-FEM captures these effects accurately, although a locally refined mesh is still required for small crack sizes or closely spaced crack tips when seeking high accuracy. In the example examining crack amplification effects, we found that SIFs at the crack tips vary with the variables c and d while maintaining a constant c/d ratio. This ratio is considered the only factor affecting SIFs under the same boundary conditions [68,69]. In the authors' perspective, this discrepancy can be attributed to the effect of the boundary, which postulates a semi-infinite medium. To substantiate this hypothesis, we extend the edge length $2a$ from 2 to 4, and employ a structured mesh with 121×121 elements for the $c = 0.05, d = 0.25$ case. This mesh discretizes the space around cracks into similarly sized elements as those in the regular mesh 61×61 in Table 2. This simple test yields $K_I^{(x=0)} = 1.1049$, a larger and more accurate value than that in the table.

We also demonstrated that DE-FEM can effectively model multiple quasi-static fracture growth without the need for local mesh refinement. In fact, the crack trajectories in Section 4.4 follow patterns akin to those reported in the literature [29,32]. These works have highlighted that coarse meshes (like the one used here) can result in wrong fracture paths. Yet, DE-FEM generates the correct paths even with the relatively coarse mesh used.

DE-FEM's enriched finite element approximation is built hierarchically on top of the standard (partition of unity) FEM shape functions, so it is possible to have multiple cracks interacting within an element—e.g., parallel cracks or a crack merging another preexisting crack. However, it is worth noting that the three-term DE-FEM approximation only includes enrichments to reproduce the kinematics of discontinuities. While the formulation is simpler than X/GFEM due to the absence of singular enrichments for capturing stress fields at crack tips, accurate stress intensity factors can still be computed; this is because SIFs converge at a rate $\mathcal{O}(h)$, which is twice as fast as that of the error in energy norm without addressing the singularity, i.e., $\mathcal{O}\left(h^{1/2}\right)$. The faster convergence of SIFs is due to functionals converging at twice the rate of their argument [71], and SIFs are computed herein by means of an interaction integral functional. We point out, however, that there is a trade-off between accuracy and ease of computer implementation, giving DE-FEM an edge over X/GFEM for the latter; in particular, we note that no special treatment is needed in DE-FEM when dealing with nonzero essential BCs and that smooth reactive tractions are recovered from immersed Dirichlet boundaries without the need for any stabilization [41]. In terms of computational cost, DE-FEM and X/FEM do not differ substantially as the effect of enrichments is only localized to cut elements. Because discontinuities are lower-dimensional geometrical manifolds, as problems increase in size, the computational cost associated with solving the linear system of equations is therefore increasingly determined by the DOFs associated with bulk finite elements. This means that, asymptotically, as problems increase in size, the computational cost of DE-FEM or X/GFEM does not differ considerably from the cost of standard FEM. In terms of stability, both DE-FEM and X/GFEM are robust as discontinuities approach nodes of the original mesh; the condition number grows at the same rate as that of standard FEM on fitted meshes, in DE-FEM by means of proper scaling [38,40,41], and in X/GFEM by means of stable formulations [72–74].

While this paper highlights the strengths of the DE-FEM approach, several challenges remain. For instance, in problems involving multiple propagating cracks, their merging could lead to fragmentation, which in turn could result in a singular stiffness matrix, as these fragments may undergo rigid-body motions. In addition, the current implementation does not account for contact when a crack closes—e.g., as the result of cyclic loading. Note, however, that our enriched formulation has already been explored for modeling contact and coupling non-conforming discretizations [75]. Furthermore, limited accuracy of linear elements in evaluating SIFs can cause fluctuations in both the energy release rate and propagation direction under mixed-mode loading, leading to inaccurate predictions of crack propagation behavior. This is evident in the oscillations observed in the reaction-COD curve of the modified CT specimen test, as shown in Fig. 10(a). If the increment is relatively large, these fluctuations can further produce a zigzag crack pattern, as illustrated in Fig. 16(b). As shown in Fig. 10(b), these oscillations are mitigated with mesh refinement due to the higher accuracy in evaluating SIFs.

The DE-FEM scheme presented for quasi-static fracture growth represents a viable alternative to other methods for modeling crack growth with complex patterns. Future extensions to the methodology can include developments to solve more challenging fracture problems, e.g., dynamic fracture, and the extension to 3-D crack growth (which can build on previous work by Zhang et al. [40,50]).

CRediT authorship contribution statement

Jujian Zhang: Writing – review & editing, Writing – original draft, Visualization, Validation, Software, Methodology, Investigation, Formal analysis, Conceptualization. **Yuheng Yan:** Software, Methodology, Conceptualization. **C. Armando Duarte:** Writing – review & editing, Formal analysis. **Alejandro M. Aragón:** Writing – review & editing, Writing – original draft, Visualization, Supervision, Software, Resources, Project administration, Methodology, Investigation, Funding acquisition, Formal analysis, Conceptualization.

Declaration of Generative AI and AI-assisted technologies in the writing process

During the preparation of this work the authors used ChatGPT to check the grammar structure of a few sentences. After using this tool, the authors reviewed and edited the content as needed and take full responsibility for the content of the publication.

Declaration of competing interest

The authors declare that they have no known competing financial interests or personal relationships that could have appeared to influence the work reported in this paper.

Appendix A. Static asymptotic field

The static asymptotic fields used in this work for the calculation of the interaction integral follow Suresh [76]:

$$u_x = \frac{K_I}{2E}\sqrt{\frac{r}{2\pi}}(1+\nu)\left[(2\kappa-1)\cos\frac{\theta}{2}-\cos\frac{3\theta}{2}\right]+\frac{K_{II}}{2E}\sqrt{\frac{r}{2\pi}}(1+\nu)\left[(2\kappa+3)\sin\frac{\theta}{2}+\sin\frac{3\theta}{2}\right] \tag{38}$$

$$u_y = \frac{K_I}{2E}\sqrt{\frac{r}{2\pi}}(1+\nu)\left[(2\kappa+1)\sin\frac{\theta}{2}-\sin\frac{3\theta}{2}\right]-\frac{K_{II}}{2E}\sqrt{\frac{r}{2\pi}}(1+\nu)\left[(2\kappa-3)\cos\frac{\theta}{2}+\cos\frac{3\theta}{2}\right] \tag{39}$$

$$\sigma_{xx} = \frac{K_I}{\sqrt{2\pi r}}\cos\frac{\theta}{2}\left(1-\sin\frac{\theta}{2}\sin\frac{3\theta}{2}\right)-\frac{K_{II}}{\sqrt{2\pi r}}\sin\frac{\theta}{2}\left(2+\cos\frac{\theta}{2}\cos\frac{3\theta}{2}\right) \tag{40}$$

$$\sigma_{yy} = \frac{K_I}{\sqrt{2\pi r}}\cos\frac{\theta}{2}\left(1+\sin\frac{\theta}{2}\sin\frac{3\theta}{2}\right)+\frac{K_{II}}{\sqrt{2\pi r}}\sin\frac{\theta}{2}\cos\frac{\theta}{2}\sin\frac{3\theta}{2} \tag{41}$$

$$\sigma_{xy} = \frac{K_I}{\sqrt{2\pi r}}\cos\frac{\theta}{2}\sin\frac{\theta}{2}\cos\frac{3\theta}{2}+\frac{K_{II}}{\sqrt{2\pi r}}\cos\frac{\theta}{2}\left(1-\sin\frac{\theta}{2}\sin\frac{3\theta}{2}\right) \tag{42}$$

where Kolosov's constant is $\kappa = \begin{cases} \frac{3-\nu}{1+\nu} & \text{for plane stress,} \\ 3-4\nu & \text{for plane strain.} \end{cases}$

The derivatives of the asymptotic displacement fields can be obtained by the chain rule, i.e.,

$$\frac{\partial u_x}{\partial x} = \frac{\partial u_x}{\partial r}\frac{\partial r}{\partial x}+\frac{\partial u_x}{\partial \theta}\frac{\partial \theta}{\partial x} \quad \text{and} \quad \frac{\partial u_y}{\partial x} = \frac{\partial u_y}{\partial r}\frac{\partial r}{\partial x}+\frac{\partial u_y}{\partial \theta}\frac{\partial \theta}{\partial x}. \tag{43}$$

Appendix B. Derivation of propagation direction θ_c with the maximum circumferential stress criterion

With the static asymptotic fields in Appendix A, the asymptotic stress fields in polar coordinates can be written as

$$\sigma_{\theta\theta} = \frac{1}{\sqrt{2\pi r}}\cos\frac{\theta}{2}\left(K_I\cos^2\frac{\theta}{2}-\frac{3}{2}K_{II}\sin\theta\right), \tag{44}$$

$$\sigma_{rr} = \frac{1}{\sqrt{2\pi r}}\cos\frac{\theta}{2}\left[K_I\left(1+\sin^2\frac{\theta}{2}\right)+\frac{3}{2}K_{II}\sin\theta-2K_{II}\tan\frac{\theta}{2}\right], \tag{45}$$

$$\sigma_{r\theta} = \frac{1}{2\sqrt{2\pi r}}\cos\frac{\theta}{2}\left[K_I\sin\theta+K_{II}(3\cos\theta-1)\right]. \tag{46}$$

The maximum circumferential stress criterion assumes the crack propagates in the direction with the largest circumferential stress $\sigma_{\theta\theta}$ and zero shear stress $\sigma_{r\theta}$. Therefore, the propagation direction θ_c satisfies the condition $\sigma_{r\theta}=0$, i.e.,

$$K_I\sin\theta_c+K_{II}\left(3\cos\theta_c-1\right)=0, \tag{47}$$

which can be expanded into:

$$K_I\tan\frac{\theta_c}{2}+K_{II}\left(1-2\tan^2\frac{\theta_c}{2}\right)=0. \tag{48}$$

The solution to this equation yields the commonly used formula (32).

Appendix C. Multiple crack coordinates

Table 3 lists all coordinates used in the multiple crack propagation example of Section 4.4.

Data availability

Data will be made available on request.

Table 3
The coordinates of the crack tips and their hierarchy.

Crack	First tip		Second tip	
	Tip	Coordinate	Tip	Coordinate
①	1	(−0.691486, 0.531184)	2	(−0.511212, 0.711458)
②	3	(−0.286790, 0.332516)	4	(−0.394709, 0.511563)
③	5	(0.128942, 0.518921)	6	(0.359495, 0.694289)
④	7	(0.673441, 0.229502)	8	(0.517694, 0.412228)
⑤	9	(−0.731955, −0.180098)	10	(−0.588472, −0.008409)
⑥	11	(−0.170287, −0.096706)	12	(0.087246, −0.042747)
⑦	13	(0.592502, −0.180098)	14	(0.456377, −0.005957)
⑧	15	(−0.673090, −0.631395)	16	(−0.517344, −0.479327)
⑨	17	(0.090925, −0.653469)	18	(−0.091801, −0.534513)
⑩	19	(0.436755, −0.635074)	20	(0.624387, −0.506307)

References

[1] N. Russo, M. Gastaldi, P. Marras, L. Schiavi, A. Strini, F. Lollini, Effects of load-induced micro-cracks on chloride penetration resistance in different types of concrete, Mater. Struct. 53 (6) (2020) 1–14.
[2] H.M. Westergaard, Bearing pressures and cracks, J. Appl. Mech. 6 (1939) A49–53.
[3] D.M. Tracey, Finite elements for determination of crack tip elastic stress intensity factors, Eng. Fract. Mech. 3 (3) (1971) 255–265.
[4] R.S. Barsoum, On the use of isoparametric finite elements in linear fracture mechanics, Internat. J. Numer. Methods Engrg. 10 (1) (1976) 25–37.
[5] M. Kuna, Finite elements in fracture mechanics: Theory-numerics-applications: Springer science & business media, 2013.
[6] A. Paluszny, R.W. Zimmerman, Numerical simulation of multiple 3D fracture propagation using arbitrary meshes, Comput. Methods Appl. Mech. Engrg. 200 (9–12) (2011) 953–966.
[7] M. Nejati, Finite Element Modeling of Frictional Contact and Stress Intensity Factors in Three-Dimensional Fractured Media Using Unstructured Tetrahedral Meshes (PhD thesis), Imperial College London, 2015.
[8] R.H.J. Peerlings, R. De Borst, W.A.M. Brekelmans, M.G.D. Geers, Localisation issues in local and nonlocal continuum approaches to fracture, Eur. J. Mech. A Solids 21 (2) (2002) 175–189.
[9] R. de Borst, C.V. Verhoosel, Damage, material instabilities, and failure, in: Encyclopedia of Computational Mechanics Second Edition, Wiley Online Library, 2018, pp. 1–50.
[10] C.V Verhoosel, M.A Scott, T.J.R. Hughes, R. De Borst, An isogeometric analysis approach to gradient damage models, Internat. J. Numer. Methods Engrg. 86 (1) (2011) 115–134.
[11] M. Ambati, T. Gerasimov, L. De Lorenzis, A review on phase-field models of brittle fracture and a new fast hybrid formulation, Comput. Mech. 55 (2015) 383–405.
[12] G.A. Francfort, J.-J. Marigo, Revisiting brittle fracture as an energy minimization problem, J. Mech. Phys. Solids 46 (8) (1998) 1319–1342.
[13] M. Buliga, Energy minimizing brittle crack propagation, J. Elasticity 52 (1998) 201–238.
[14] G. Dal Maso, R. Toader, A model for the quasi-static growth of brittle fractures: Existence and approximation results, Arch. Ration. Mech. Anal. 162 (2002) 101–135.
[15] B. Bourdin, G.A. Francfort, J.-J. Marigo, Numerical experiments in revisited brittle fracture, J. Mech. Phys. Solids 48 (4) (2000) 797–826.
[16] B. Bourdin, G.A. Francfort, J.-J. Marigo, The variational approach to fracture, J. Elasticity 91 (2008) 5–148.
[17] C. Miehe, M. Hofacker, F. Welschinger, A phase field model for rate-independent crack propagation: Robust algorithmic implementation based on operator splits, Comput. Methods Appl. Mech. Engrg. 199 (45–48) (2010) 2765–2778.
[18] C. Miehe, F. Welschinger, M. Hofacker, Thermodynamically consistent phase-field models of fracture: Variational principles and multi-field FE implementations, Int. J. Numer. Methods Eng. 83 (10) (2010) 1273–1311.
[19] C. Miehe, S. Mauthe, Phase field modeling of fracture in multi-physics problems. Part III. Crack driving forces in hydro-poro-elasticity and hydraulic fracturing of fluid-saturated porous media, Comput. Methods Appl. Mech. Engrg. 304 (2016) 619–655.
[20] L. Chen, Z. Wang, B. Li, R. de Borst, Computation of the crack opening displacement in the phase-field model, Int. J. Solids Struct. (2023) 112496.
[21] A. Portela, M.H. Aliabadi, D.P. Rooke, Dual boundary element incremental analysis of crack propagation, Comput. Struct. 46 (2) (1993) 237–247.
[22] T. Belytschko, Y.Y. Lu, L. Gu, Element-free Galerkin methods, Int. J. Numer. Methods Eng. 37 (2) (1994) 229–256.
[23] T. Belytschko, Y.Y. Lu, L. Gu, Crack propagation by element-free Galerkin methods, Eng. Fract. Mech. 51 (2) (1995) 295–315.
[24] T. Belytschko, T. Black, Elastic crack growth in finite elements with minimal remeshing, Int. J. Numer. Methods Eng. 45 (5) (1999) 601–620.
[25] N. Moës, J. Dolbow, T. Belytschko, A finite element method for crack growth without remeshing, Int. J. Numer. Methods Eng. 46 (1) (1999) 131–150.
[26] C.A. Duarte, O.N. Hamzeh, T.J. Liszka, W.W. Tworzydlo, A generalized finite element method for the simulation of three-dimensional dynamic crack propagation, Comput. Methods Appl. Mech. Engrg. 190 (15–17) (2001) 2227–2262.
[27] T. Belytschko, H. Chen, J. Xu, G. Zi, Dynamic crack propagation based on loss of hyperbolicity and a new discontinuous enrichment, Int. J. Numer. Methods Eng. 58 (12) (2003) 1873–1905.
[28] J. Réthoré, A. Gravouil, A. Combescure, An energy-conserving scheme for dynamic crack growth using the extended finite element method, Internat. J. Numer. Methods Engrg. 63 (5) (2005) 631–659.
[29] E. Budyn, G. Zi, N. Moës, T. Belytschko, A method for multiple crack growth in brittle materials without remeshing, Int. J. Numer. Methods Eng. 61 (10) (2004) 1741–1770.
[30] S. Loehnert, T. Belytschko, A multiscale projection method for macro/microcrack simulations, Internat. J. Numer. Methods Engrg. 71 (12) (2007) 1466–1482.
[31] P. O'Hara, C.A. Duarte, T. Eason, A two-scale generalized finite element method for interaction and coalescence of multiple crack surfaces, Eng. Fract. Mech. 163 (2016) 274–302.
[32] J. Ding, T. Yu, Y. Yang, T.Q. Bui, An efficient variable-node XFEM for modeling multiple crack growth: A Matlab object-oriented implementation, Adv. Eng. Softw. 140 (2020) 102750.

[33] F. Xu, H. Hajibeygi, L.J. Sluys, Adaptive multiscale extended finite element method (MS-XFEM) for the simulation of multiple fractures propagation in geological formations, J. Comput. Phys. 486 (2023) 112114.
[34] C. Daux, N. Moës, J. Dolbow, N. Sukumar, T. Belytschko, Arbitrary branched and intersecting cracks with the extended finite element method, Int. J. Numer. Methods Eng. 48 (12) (2000) 1741–1760.
[35] G. Zi, J.-H. Song, E. Budyn, S.-H. Lee, T. Belytschko, A method for growing multiple cracks without remeshing and its application to fatigue crack growth, Modelling Simul. Mater. Sci. Eng. 12 (5) (2004) 901.
[36] A.M. Aragón, C.A. Duarte, Fundamentals of Enriched Finite Element Methods, first ed., Elsevier, 2023.
[37] S. Soghrati, A.M. Aragón, C.A. Duarte, P.H. Geubelle, An interface-enriched generalized FEM for problems with discontinuous gradient fields, Int. J. Numer. Methods Eng. 89 (8) (2012) 991–1008.
[38] A.M. Aragón, B. Liang, H. Ahmadian, S. Soghrati, On the stability and interpolating properties of the hierarchical interface-enriched finite element method, Comput. Methods Appl. Mech. Engrg. 362 (2020) 112671.
[39] A.M. Aragón, A. Simone, The discontinuity-enriched finite element method, Internat. J. Numer. Methods Engrg. 112 (11) (2017) 1589–1613.
[40] J. Zhang, S.J. van den Boom, F. van Keulen, A.M. Aragón, A stable discontinuity-enriched finite element method for 3-D problems containing weak and strong discontinuities, Comput. Methods Appl. Mech. Engrg. 355 (2019) 1097–1123.
[41] S.J. van den Boom, J. Zhang, F. van Keulen, A.M. Aragón, A stable interface-enriched formulation for immersed domains with strong enforcement of essential boundary conditions, Internat. J. Numer. Methods Engrg. 120 (10) (2019) 1163–1183.
[42] E. De Lazzari, S.J. van den Boom, J. Zhang, F. van Keulen, A.M. Aragón, A critical view on the use of non-uniform rational b-splines to improve geometry representation in enriched finite element methods, Internat. J. Numer. Methods Engrg. 122 (5) (2021) 1195–1216.
[43] D. Liu, J. Zhang, A.M. Aragón, A. Simone, The discontinuity-enriched finite element method for multiple intersecting discontinuities, Comput. Methods Appl. Mech. Engrg. 433 (2025) 117432.
[44] S. van Bergen, R.A. Norte, A.M. Aragón, An interface-enriched generalized finite element method for the analysis and topology optimization of 2-D electromagnetic problems, Comput. Methods Appl. Mech. Engrg. 421 (2024) 116748.
[45] S.J. van den Boom, J. Zhang, F. van Keulen, A.M. Aragón, An interface-enriched generalized finite element method for level set-based topology optimization, Struct. Multidiscip. Optim. 63 (1) (2021) 1–20.
[46] A.A. Griffith, VI. The phenomena of rupture and flow in solids, Philos. Trans. R. Soc. Lond. Ser. A Math. Phys. Eng. Sci. 221 (582–593) (1921) 163–198.
[47] F. Erdogan, G.C. Sih, On the crack extension in plates under plane loading and transverse shear, 1963.
[48] G.C. Sih, Strain-energy-density factor applied to mixed mode crack problems, Int. J. Fract. 10 (1974) 305–321.
[49] C.H. Wu, Maximum-energy-release-rate criterion applied to a tension-compression specimen with crack, J. Elasticity 8 (3) (1978) 235–257.
[50] J. Zhang, E. Zhebel, S.J van den Boom, D. Liu, A.M. Aragón, An object-oriented geometric engine design for discontinuities in unfitted/immersed/enriched finite element methods, Internat. J. Numer. Methods Engrg. 123 (21) (2022) 5126–5154.
[51] J.R. Rice, A path independent integral and the approximate analysis of strain concentration by notches and cracks, 1968.
[52] C.F. Shih, R.J. Asaro, Elastic-plastic analysis of cracks on bimaterial interfaces: part I—small scale yielding, 1988.
[53] G.R. Irwin, Analysis of stresses and strains near the end of a crack traversing a plate, 1957.
[54] M. Negri, C. Ortner, Quasi-static crack propagation by Griffith's criterion, Math. Models Methods Appl. Sci. 18 (11) (2008) 1895–1925.
[55] A.C. Correas, J. Reinoso, P. Cornetti, M. Corrado, On the (lack of) representativeness of quasi-static variational fracture models for unstable crack propagation, J. Mech. Phys. Solids 186 (2024) 105573.
[56] C. Hou, X. Jin, X. Fan, R. Xu, Z. Wang, A generalized maximum energy release rate criterion for mixed mode fracture analysis of brittle and quasi-brittle materials, Theor. Appl. Fract. Mech. 100 (2019) 78–85.
[57] F.M. Mukhtar, P.D. Alves, C.A. Duarte, Validation of a 3-D adaptive stable generalized/extended finite element method for mixed-mode brittle fracture propagation, Int. J. Fract. 225 (2) (2020) 129–152.
[58] K.H. Pham, K. Ravi-Chandar, C.M. Landis, Experimental validation of a phase-field model for fracture, Int. J. Fract. 205 (2017) 83–101.
[59] C.F. Shih, Relationships between the J-integral and the crack opening displacement for stationary and extending cracks, J. Mech. Phys. Solids 29 (4) (1981) 305–326.
[60] A.R. Ingraffea, M. Grigoriu, Cornell Univ Ithaca Ny Dept of Structural Engineering, Probabilistic fracture mechanics: A validation of predictive capability, 1990.
[61] T.N. Bittencourt, P.A. Wawrzynek, A.R. Ingraffea, J.L. Sousa, Quasi-automatic simulation of crack propagation for 2D LEFM problems, Eng. Fract. Mech. 55 (2) (1996) 321–334.
[62] Z. Kang, T.Q. Bui, T. Saitoh, S. Hirose, Quasi-static crack propagation simulation by an enhanced nodal gradient finite element with different enrichments, Theor. Appl. Fract. Mech. 87 (2017) 61–77.
[63] B. Giovanardi, A. Scotti, L. Formaggia, A hybrid XFEM–phase field (xfield) method for crack propagation in brittle elastic materials, Comput. Methods Appl. Mech. Engrg. 320 (2017) 396–420.
[64] F. Cazes, N. Moës, Comparison of a phase-field model and of a thick level set model for brittle and quasi-brittle fracture, Internat. J. Numer. Methods Engrg. 103 (2) (2015) 114–143.
[65] B. A. Szabo, I. Babuška, Computation of the amplitude of stress singular terms for cracks and reentrant corners, in: Fracture Mechanics: Nineteenth Symposium, ASTM International, 1988.
[66] J.P. Pereira, C.A. Duarte, Extraction of stress intensity factors from generalized finite element solutions, Eng. Anal. Bound. Elem. 29 (4) (2005) 397–413.
[67] P. Gupta, C.A. Duarte, A. Dhankhar, Accuracy and robustness of stress intensity factor extraction methods for the generalized/eXtended Finite Element Method, Eng. Fract. Mech. 179 (2017) 120–153.
[68] A.A. Rubinstein, Macrocrack interaction with semi-infinite microcrack array, Int. J. Fract. 27 (1985) 113–119.
[69] L.R.F. Rose, Microcrack interaction with a main crack, Int. J. Fract. 31 (1986) 233–242.
[70] S. Loehnert, T. Belytschko, Crack shielding and amplification due to multiple microcracks interacting with a macrocrack, Int. J. Fract. 145 (2007) 1–8.
[71] I. Babuška, A. Miller, The post-processing approach in the finite element method—Part 2: The calculation of stress intensity factors, Internat. J. Numer. Methods Engrg. 20 (6) (1984/06/01) 1111–1129.
[72] I. Babuška, U. Banerjee, Stable generalized finite element method (SGFEM), Comput. Methods Appl. Mech. Engrg. 201 (2012) 91–111.
[73] A.G. Sanchez-Rivadeneira, C.A. Duarte, A stable generalized/eXtended FEM with discontinuous interpolants for fracture mechanics, Comput. Methods Appl. Mech. Engrg. 345 (2019) 876–918.
[74] A.G. Sanchez-Rivadeneira, N. Shauer, B. Mazurowski, C.A. Duarte, A stable generalized/eXtended p-hierarchical FEM for three-dimensional linear elastic fracture mechanics, Comput. Methods Appl. Mech. Engrg. 364 (2020) 112970.
[75] D. Liu, S.J. van den Boom, A. Simone, A.M. Aragón, An interface-enriched generalized finite element formulation for locking-free coupling of non-conforming discretizations and contact, Comput. Mech. 70 (3) (2022) 477–499.
[76] S. Suresh, Fatigue of materials, Cambridge University Press, 1998.